Draft version March 19, 2021
Typeset using LaTeX **twocolumn** style in AASTeX63

Joint Survey Processing I: Compact oddballs in the COSMOS field – low-luminosity Quasars at $z > 6$?

Andreas L. Faisst [1], Ranga Ram Chary [1], Sergio Fajardo-Acosta [1], Roberta Paladini [1], Benjamin Rusholme [1], Nathaniel Stickley [1], George Helou [1], John R. Weaver [2,3], Anton M. Koekemoer [4] and Hironao Miyatake [5,6,7]

[1] *Caltech/IPAC, MS314-6, 1200 E. California Blvd. Pasadena, CA 91125, USA*
[2] *Cosmic Dawn Center (DAWN)*
[3] *Niels Bohr Institute, University of Copenhagen, Jagtvej 128, 2200 Copenhagen, Denmark*
[4] *Space Telescope Science Institute, 3700 San Martin Dr., Baltimore, MD 21218, USA*
[5] *Institute for Advanced Research, Nagoya University, Nagoya 464-8601, Japan*
[6] *Division of Particle and Astrophysical Science, Graduate School of Science, Nagoya University, Nagoya 464-8602, Japan*
[7] *Kavli Institute for the Physics and Mathematics of the Universe (Kavli IPMU, WPI), University of Tokyo, Chiba 277-8582, Japan*

(Received -; Revised -; Accepted -)

Submitted to ApJ

ABSTRACT

The faint-end slope of the quasar luminosity function at $z \sim 6$ and its implication on the role of quasars in reionizing the intergalactic medium at early times has been an outstanding problem for some time. The identification of faint high-redshift quasars with luminosities of $< 10^{44.5}$ erg s^{-1} is challenging. They are rare (few per square degree) and the separation of these unresolved quasars from late-type stars and compact star-forming galaxies is difficult from ground-based observations alone. In addition, source confusion becomes significant at > 25 mag, with $\sim 30\%$ of sources having their flux contaminated by foreground objects when the seeing resolution is $\sim 0.7''$. We mitigate these issues by performing a pixel-level joint processing of ground and space-based data from Subaru/*HSC* and *HST*/ACS. We create a deconfused catalog over the 1.64 deg^2 of the COSMOS field, after accounting for spatial varying PSFs and astrometric differences between the two datasets. We identify twelve low-luminosity ($M_{UV} \sim -21$ mag) $z > 6$ quasar candidates through *(i)* their red color measured between ACS/F814W and HSC/i-band and *(ii)* their compactness in the space-based data. We estimate that late-type stars could contribute up to $\sim 50\%$ to our sample. Our constraints on the faint end of the quasar luminosity function at $z \sim 6.4$ suggests a negligibly small contribution to reionization compared to the star-forming galaxy population. The confirmation of our candidates and the evolution of number density with redshift could provide better insights into how supermassive galaxies grew in the first billion years of cosmic time.

Keywords: Surveys (1671), Quasars (1319), High-redshift galaxies (734), Photometry (1234), Astronomical techniques (1684)

1. INTRODUCTION

Quasi-stellar objects (QSOs) or quasars, are powered by accretion of gas on to a supermassive ($> 10^9\,M_\odot$) black hole. Since the detection of luminous quasars within the first Gyr ($z > 6$) of the Big Bang using wide-area surveys such as the Sloan Digital Sky Survey, PanSTARRS, CFHTLS and VIDEO/VIKING (Fan et al. 2001; Becker et al. 2001; Bañados et al. 2016; McGreer et al. 2018), it has been challenging to explain their origin and existence. Have their central engines built up their mass through sporadic, Eddington-limited accretion of gas or do they build up through more continuous accretion processes onto a relatively massive

Corresponding author: Andreas L. Faisst
afaisst@ipac.caltech.edu

black hole seed (Bañados et al. 2018; Trakhtenbrot et al. 2017)? If so, are the massive black hole seeds primordial in nature or are they end stages of early epochs of massive star-formation? Tracing the evolution of the quasar luminosity function, particularly at the low luminosity end, at the earliest cosmic times can potentially shed light on the origin of these systems. In addition, studying the number of quasars in the early Universe can help quantify their contribution to the reionization of the Universe (See e.g. Fan et al. 2006).

While identification and spectroscopic confirmation of luminous $z \sim 6$ quasars has become relatively straightforward, measuring the faint end ($< 10^{44.5}$ erg s^{-1}) of the quasar luminosity function is much more challenging. First, identification of faint quasars requires a significant color difference across the Lyman-break/Lyα forest. This implies that in order to measure the break, the blue band must be at least a magnitude more sensitive. Second, faint quasars are point sources and can lack multi-wavelength information due to the sensitivity differences between the different bands. They can be mistaken as either late-type stars in the local Universe or compact, strong emission line galaxies at intermediate redshifts. This is especially true at seeing-limited spatial resolution of $\sim$0.7″. Space-resolution data with <0.1″ seeing can help avoid this mis-identification but wide-area surveys from space at such resolution are not yet available except in the COSMOS field with the *Hubble* Space Telescope (Scoville et al. 2007; Koekemoer et al. 2007). The combined analysis of ground- and space-based data is therefore crucial to be able to robustly identify candidate, low-luminosity QSOs.

The next problem arises due to source confusion. At optical wavelengths, the classical confusion limit at seeing limited resolution is 25 AB mag (5×10^{44} erg s^{-1} at $z \sim 6$ is 25 AB mag) as estimated from source counts estimates from pencil beam surveys. From this we can estimate that the brightness of $\sim$30% of the fainter objects are contaminated by the presence of a neighboring brighter source. This makes it challenging to reliably measure colors or color limits for the sources. Disentangling the relative contributions of the confusing sources requires priors from deep, higher spatial resolution data and joint pixel level processing, taking into account accurate astrometry, and accurate position/source-dependent point spread functions; this is beyond the capability of current cataloging algorithms.

Future deep, wide-area surveys conducted from space using the *Euclid* and the *Nancy Grace Roman* space telescopes as well as from the ground using the *Vera C. Rubin* observatory are well in the regime of deep, confusion-limited, wide-area imaging. Although they promise to push the identification and characterization of *luminous* quasars out to redshifts beyond $z = 8$, the infrastructure for precise, joint analysis of those datasets does not yet exist.

In this paper, we demonstrate the scientific benefits of joint pixel level processing over the relatively small area of 1.6 square degrees, to assess the faint end of the QSO luminosity function at $z \sim 6$. We combine two data sets that are very similar to the future surveys. These are the Subaru/Hyper-SuprimeCam (HSC) i-band survey (Aihara et al. 2018) and the 2004 *Hubble*/ACS F814W imaging survey on the roughly 2 deg^2 COSMOS field (Scoville et al. 2007; Koekemoer et al. 2007). These data have similar seeing and point-spread function (PSF) properties as future *Rubin* and *Roman/Euclid* imaging observations.

This paper is structured as follows. In Section 2, we present in detail the different datasets used and their preparation (astrometric calibration and PSF). In Section 3, we detail the generation of a photometry catalog based on a joint modeling of the ACS and HSC images. Specifically, we use the high-resolution ACS images as priors to mitigate blending and confusion issues in the HSC data. In Section 4, we present the sample selection and discuss different possible contamination of our sample. We discuss our results in Section 5 and conclude in Section 6.

Throughout this work, we assume a ΛCDM cosmology with $H_0 = 70\,\mathrm{km\,s^{-1}\,Mpc^{-1}}$, $\Omega_\Lambda = 0.7$, and $\Omega_\mathrm{m} = 0.3$. All magnitudes are given in the AB system (Oke 1974) and stellar masses and star formation rates (SFRs) are normalised to a Chabrier (2003) initial mass function (IMF).

2. DATASETS AND PREPARATION

2.1. *Imaging Data*

Identification of faint, $z \sim 6$ QSOs requires having adequately deep imaging data for selection using the Lyman-break technique (e.g., Steidel et al. 1996). Furthermore, we need at least one band to have high spatial resolution so that a separation between resolved galaxies and point-like quasars is possible. We use the *Hubble*/ACS F814W data (Scoville et al. 2007; Koekemoer et al. 2007) and the 2018 data release 1 (Aihara et al. 2018) of the Hyper-SuprimeCam (HSC) $i-$band ultra-deep data from the *Subaru* Strategic Program (SSP) survey in COSMOS. As shown in Figure 1, the bandpasses and depths of these datasets are well matched, allowing for the selection of red objects between $5.9 < z < 6.7$. The ACS data were taken between 2003 Oct 15 and 2005

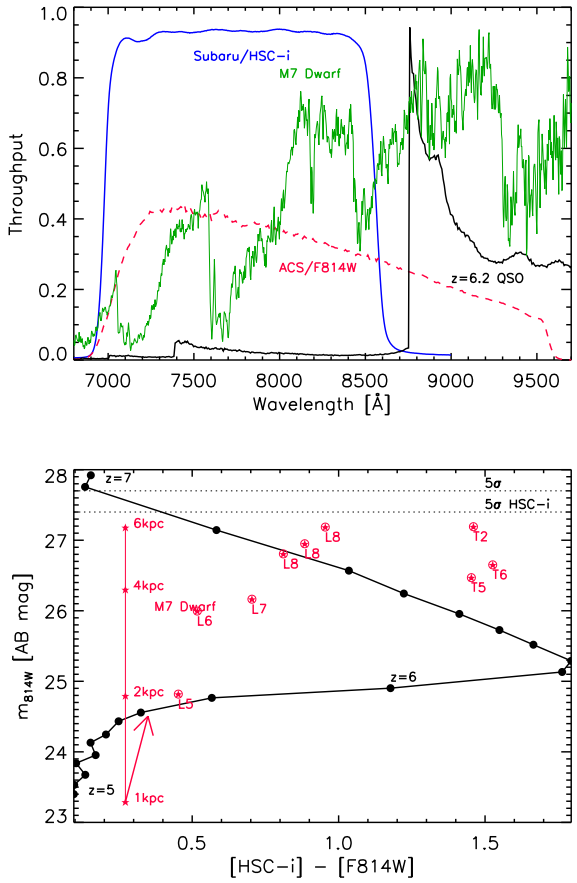

Figure 1. $z \sim 6$ quasars can be selected through a color difference between photometry in the *Subaru*/HyperSuprimeCam $i-$band and the *Hubble*/ACS F814W filter. **Top:** Comparison between the HSC i-band (blue solid) and ACS/F814W filter (red dashed) throughput curves. The F814W extends to the red, hence the flux difference acts similarly to a narrow-band filter. The black line shows an average quasar template from Vanden Berk et al. (2001) redshifted to $z = 6.2$ with absorption by the intergalactic medium applied. We also show the spectrum of an M7 brown dwarf from Fajardo-Acosta et al. (2016) as comparison (green). **Bottom:** Expected [HSC-i]−[F814W] color for the average quasar template at redshifts $z = 5 - 7$ and normalized to a $B-$band luminosity of $10^{45}\,\mathrm{erg\,s^{-1}}$ (black line and dots). For galaxies and quasars at $5.9 < z < 6.8$, the [HSC-i]−[F814W] colors will be > 0.5 mag mainly due to absorption by the Lyman-α forest blueward of 1215 Å as well as the Lyα emission line. The red symbols denote different spectral types of brown dwarfs at their native distances from DwarfArchives.org. The red line shows the M7 dwarf from the top panel at distances between $1 - 6$ kpc. The impact of a $A_V = 2$ mag extinction on the stellar spectra is shown by the red arrow. We discuss the contamination by stars in Section 4.5 in more detail.

May 21 while the HSC data were taken between 2014 March and 2015 November. Stellar proper motions result in significant astrometric mismatches between these datasets which need to be corrected for. Furthermore, these data have not been aligned to the *Gaia* astrometric reference frame, which needs to be remedied.

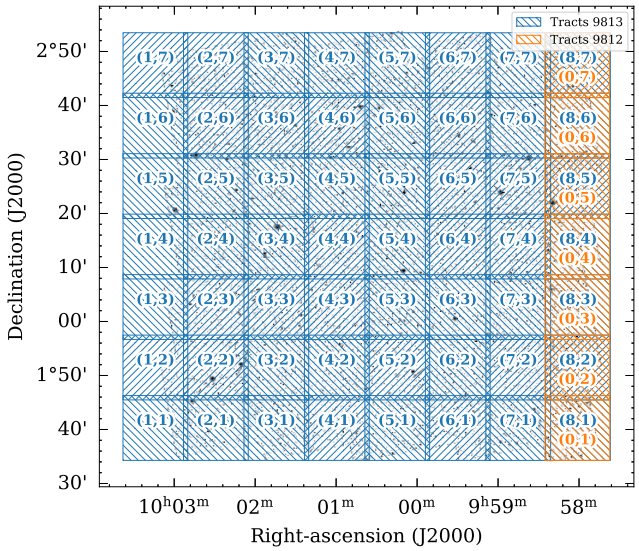

Figure 2. Spatial organization of *patches* on the COSMOS field. Shown are only the 63 $12' \times 12'$ *patches* overlapping with the ACS/F814W observations (gray scale, background). COSMOS is covered by *tract* 9813 (blue) but also has a small coverage from *tract* 9812 (orange). The *patch* numbers are indicated as (X,Y) pairs. Each of the *patches* are divided into 9 *sub-patches* (size $3''$) to facilitate multi-processor computing.

We start with the v2.0 ACS mosaics available within the Infrared Science Archive (IRSA[1]), which have a PSF full width at half maximum (FWHM) of $0.095''$ and a spatial scale of 30 mas/pixel (Koekemoer et al. 2007). In contrast, the HSC data have a PSF FWHM between 0.6-0.9″ and a spatial scale of 168 mas/pixel (Aihara et al. 2018).

The F814W bandpass overlaps entirely with the Subaru/HSC i-band filter and extends redward (see Section 4.1). This allows high-z sources (at a median $z \sim 6.4$) to be selected based on a large color difference in these bandpasses. This acts similar to selection in a narrow-band filter. The sensitivity of the surveys should allow the detection of objects down to $M_{UV} = -22.1$ mag, at least $3-4$ mags deeper than DESI Legacy imaging surveys, over much smaller areas (Dey et al. 2019), with the added advantage of high spatial resolution in one of the bands.

2.2. *Data Organization Terminology*

[1] https://irsa.ipac.caltech.edu/Missions/cosmos.html

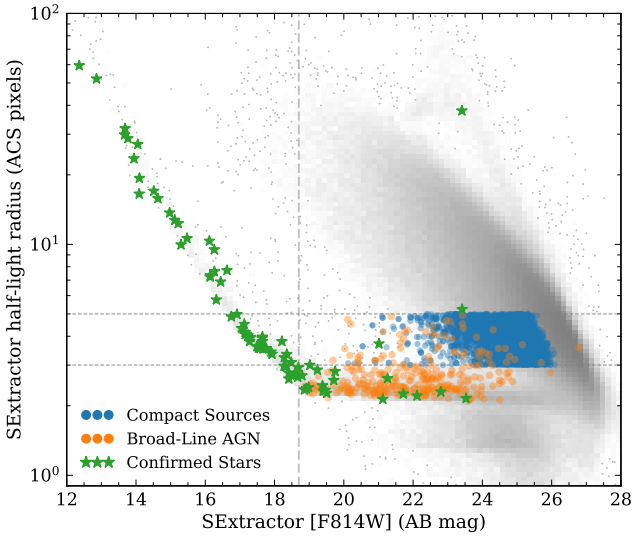

Figure 3. Selection of compact sources (blue) for astrometric calibration of imaging data. Also shown are confirmed broad-line AGN (orange, Marchesi et al. 2016; Civano et al. 2016; Lanzuisi et al. 2018a) and spectroscopically confirmed stars (green). The *gray* symbols ("background cloud") are all the objects in COSMOS. The "stellar locus," where point sources lie, is horizontal from right to left, and turns up around 18.7 mag (indicated by the *vertical dashed line*), which is the magnitude where point sources become saturated. The horizontal *dashed lines* indicate sizes of 3 and 5 ACS pixels. See text for more details on the selection of compact sources.

For efficient handling and computing of joint catalogs between these datasets which are a total of ∼1 TB, we organized the data in *tracts*, *patches*, and *sub-patches*. The HSC data is organized in 1.7 deg × 1.7 deg *tracts*. Each of them is split in 81 $12' \times 12'$ *patches* (see Aihara et al. 2018). The *tracts* have a $1'$ overlapping region, while the *patches* overlap within 100 px, which corresponds to $16.8''$. The *patches* themselves are stacks of different visits.

The ACS observations on the COSMOS field are covered by *tract* numbers 9812 and 9813, including 63 *patches* of the total 133 *patches* contained in the ultra-deep data. To allow multi-processing of these data in the following, we cut the *patches* into 16 *sub-patches* of size $3' \times 3'$ and overlap of $10''$. Hence, in total there are 1008 *sub-patches* to be processed (Figure 2).

While the HSC images are already cut into *patches*, we scripted a Python wrapper to use the online IRSA cutout tool[2] to cut and retrieve the ACS images at the correct size and location from the IRSA server. The *sub-patches* are then created using the `Cutout2D` Python package provided by *Astropy*[3] (Astropy Collaboration et al. 2013, 2018).

2.3. *Astrometric Calibration of Imaging Data*

The alignment of images (i.e., their relative astrometric calibration) is crucial to perform any successful joint pixel level processing. Among others, an accurate astrometric calibration of the images allows us to use the ∼ 11 year time baseline between ACS and HSC data to study the proper motions of faint stars (see Fajardo-Acosta et al. 2021). For this work, an accurate relative astrometric calibration is needed to use the priors on location and sizes from the *Hubble*/ACS imaging, to mitigate the effects of blending and confusion in ground based images (see Section 3). The HSC data used here had been aligned with PanSTARRS DR1, while the astrometric reference frame for the ACS data was defined by CFHT $i-$band mosaics (Capak et al. 2007) that covered the full COSMOS field to a 5σ limiting depth of 26.2 mag. It provided ∼ 300-600 sources on each ACS tile, that could be used for relative registration. Each ACS tile was then registered to the CFHT grid, and the overall relative alignment precision was found to be ∼ 5-10 milliarcseconds (see also Koekemoer et al. 2011). However, this relative precision between the ACS and the CFHT sources does not account for possible absolute errors in the CFHT astrometry, which we explore.

We use two methods to align the images *patch* by *patch*. In the first method, we compute the absolute astrometric alignment of the images using 3937 stars from the *Gaia* DR2 catalog (Lanzuisi et al. 2018b), matched to ACS sources within a 0.2 arcsec radius. Since Gaia stars are generally bright, saturation is an issue especially for the deep ground and space-based images used here. We run SExtractor (Bertin & Arnouts 1996) on the ACS images to generate a catalog with approximate source sizes. We define a "stellar locus" in a magnitude vs size plot as shown in Figure 3. Typically, stars would be unresolved and would have FWHM sizes of ∼2-3 ACS pixels. However, bright/saturated stars have a larger fraction of their point spread function profile above the noise threshold which is the reason for the size increasing as a function of brightness. From the upturn of the "stellar locus" on this diagram, as well as Gaussian fits to individual stars, we estimate a saturation threshold of about 18.7 mag. The faintest Gaia stars in our ACS sample were 20.9 mag in our catalog and so we use sources in the magnitude range $18.7 - 20.9$ mag which

[2] https://irsa.ipac.caltech.edu/data/COSMOS/index_cutouts.html

[3] http://www.astropy.org

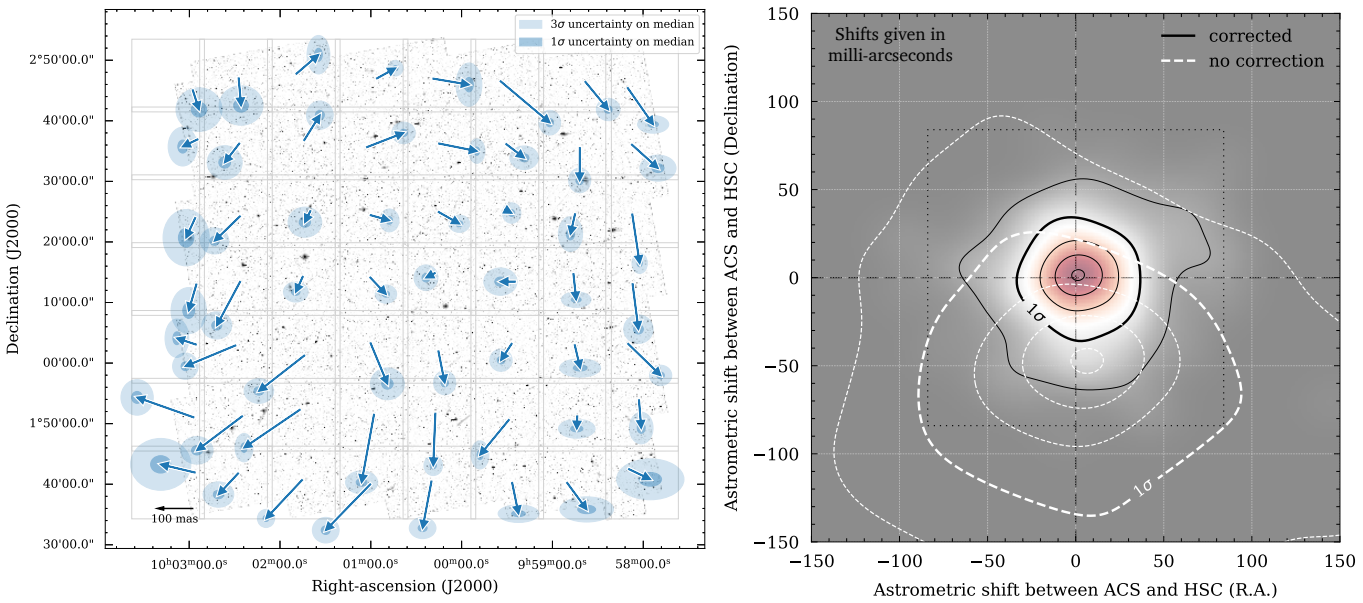

Figure 4. Astrometric calibration of ACS and HSC images. *Left:* Astrometric offset between ACS (from Koekemoer et al. (2007), originally registered ot the ground-based astrometric catalog from Capak et al. (2007)) and HSC, for each of the $12' \times 12'$ *patches*. The ellipses show 1σ and 3σ uncertainties in the direction and length of the vectors. The 100 mas length is shown on the lower left. *Right:* Accuracy of astrometric corrections (in milli-arcseconds) tested on a sample of 150 spectroscopically confirmed broad-line AGN (Marchesi et al. 2016; Civano et al. 2016; Lanzuisi et al. 2018a). The white contours show the distribution of the astrometric offsets between ACS and HSC before correction. The black contours show the offset after applying the corrections. We find no significant residual offset, and the accuracy is $\sim 30 - 40$ mas.

have less than 3 pixels half light radius, to estimate the astrometry. We identified the positions of these objects on the HSC images using 2-dimensional Gaussian fits. This was not necessary for the ACS images because the centroiding accuracy is much smaller than the typical astrometric scatter that we expect. For each of the different *patches*, we then computed the true position of the *Gaia* stars from their DR2 catalog proper motion. While the epochs of the HSC images are within 2015 (close to the epoch of *Gaia*, 2015.5), the ACS images were taken between 2003 and 2005. We therefore compute the mean epoch of each ACS source from the individual exposures that covered it. For HSC, all sources within a *patch* were measured simultaneously. The mean of the offsets between true and measured positions of the *Gaia* stars are then used to compute the astrometric offset between ACS and HSC of a given *patch*.

For the second method, we use compact extra-galactic sources on both images to compute their relative astrometric offset (Figure 3). Ideally, one would use quasars or AGN for this, as they are point sources and do not have proper motions. However, the density of bright quasars is less than a few per square degree. Instead, we select our compact sources to have *(i)* a minor-to-major (B/A) axis ratio of more than 0.9 on the ACS images, *(ii)* a signal-to-noise (S/N) ratio of more than 25 in ACS, *(iii)* an ACS magnitude fainter than 20 mag, and *(iv)* sizes between 3 and 5 ACS pixels (corresponding to $0.09'' - 0.15''$). In addition, we avoid blended sources by restricting the sample to those with SExtractor flag `FLAG`$= 0$. Finally, we apply a S/N threshold of 10 for their HSC photometry. In total, we select about 5000 compact sources. Their position on the HSC and ACS images are then compared to compute the astromeric offset between these images.

We find that both methods lead to similar astrometric offsets (within $\sim 3 - 5$ mas) and therefore choose to use the second method in what follows. Furthermore, we note that some of the bright Gaia stars could be in the non-linear/saturation regime even at 20 mag. This could potentially effect the astrometric correction. However, since we find almost identical astrometric offsets using Gaia stars and faint compact sources, we think that this effect is negligible.

The left panel of Figure 4 shows the average relative astrometric offset between ACS and HSC images per $12' \times 12'$ *patch*. The ellipses show the 1σ and 3σ uncertainties in direction, and the length of a 100 mas shift is indicated on the lower left. Note the clear clock-wise circular pattern that could be due to inhomogeneous astrometric calibration due to distortions on either the ACS or HSC images. Subsequent data releases both by HSC and a re-reduction of the ACS data (G. Brammer et al., private communication) have fixed these offsets

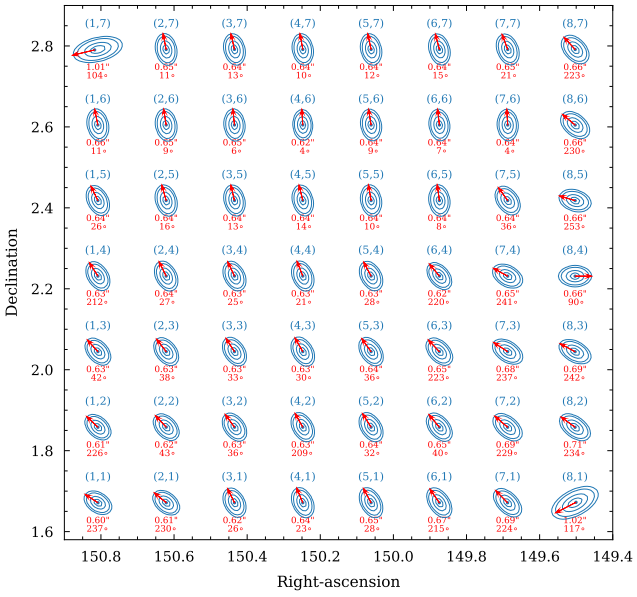

Figure 5. Variations in the HSC PSF across the COSMOS field. Generally, the variations are on a very small level, however we notice that the PSFs have a preferred north-south direction (ellipticity exagerated by 50%). The contours show the 20%, 50%, 80%, and 90% enclosed flux of the PSF. The red arrows show the semi-major axis (with FWHM and position angle indicated). The *patch* numbers are indicated in blue.

but at the time this work was initiated, these astrometric offsets were present.

The right panel of Figure 4 is an assessment of the accuracy of our astrometric calibration. Specifically, we apply the astrometric shifts to a sample of 150 spectroscopically confirmed broad-line AGN (see Figure 3; Marchesi et al. 2016; Civano et al. 2016; Lanzuisi et al. 2018a). These are point sources and do not have proper motions, hence are ideal to test the astrometric calibration. The white contours show the shift in R.A. and Declination before applying the astrometric correction between HSC and ACS. The black contours show the distribution after correction. It is centered at zero (as it should be because AGN do not have motions) with a 1σ width of $30-40$ mas. The latter is our precision of astrometric calibration. For more details, we refer to our companion paper on proper motion of faint stars by Fajardo-Acosta et al. (2021). We anticipate that in space-based data with larger fields of view resulting in higher source numbers, the astrometric precision can be improved further by at least a factor of two.

2.4. *PSF estimation*

In addition to the astrometry, the PSF of both HSC and ACS images has to be known accurately in order to produce reliable photometry. To create a spatially varying PSF, we stack unsaturated *Gaia* stars as well as fainter stars. We select the latter on the ACS images by extrapolating the "stellar locus", fit by the *Gaia* stars on the magnitude vs. size diagram (Figure 3), to lower magnitudes of 23 mag. To create the stacks, we use the code `PSFex` (Bertin 2011), which creates a magnitude-dependent model PSF based on a linear combination of (sub-pixel centered) stars in a given catalog. It also outputs the residual after subtracting a scaled PSF for each of the stars in the sample, which is useful to access the quality of the fits. We found that the residuals are smaller by a few percent for a magnitude dependent fit compared to a simple stack. Depending on the ACS coverage, we are able to use between 30 and 100 stars per $12' \times 12'$ *patches* for the fit. The ACS PSF FWHM is less than $0.1''$, while the HSC PSF FWHM varies between $0.60''$ and $0.75''$ with a median around $0.64''$. We find that the HSC PSFs have a preferred direction, which is approximately north-south. Other variations in rotation and ellipticity between the different *patches* are relatively minor but nonetheless have to be taken into account to measure robust photometry (Figure 5).

3. JOINT CATALOGING WITH TRACTOR

Once the astrometric offset between the ground- and space-based data set is established, and the PSF for each dataset calculated, we can undertake joint pixel-level photometry. This takes into account the location and morphological extent of the sources in the space-resolution data to alleviate the role of source confusion and accurately measure the photometry in the ground-based data. Here we use the code Tractor[4] (Lang et al. 2016a,b; Weaver et al. 2021a).

In brief, Tractor performs a parametric shape fit to a source in an image by using a maximum likelihood analysis including its weight map. Thereby multiple sources can be fit simultaneously on an image, which is the preferred way to run Tractor to obtain robust photometric measurements (see also detailed description and testing in Weaver et al. 2021b).

Tractor has two major advantages compared to classical photometry codes such as SExtractor or other aperture-based methods. First, it can use shape priors derived from a high-resolution image to photometer low-resolution images. To do so, Tractor can be forced to fix the shape and position and only vary the normalization (i.e., total flux) to minimize the residuals. In bands such as the HSC$-i$ and ACS F814W which are overlapping, this is a reasonable assumption

[4] http://thetractor.org/

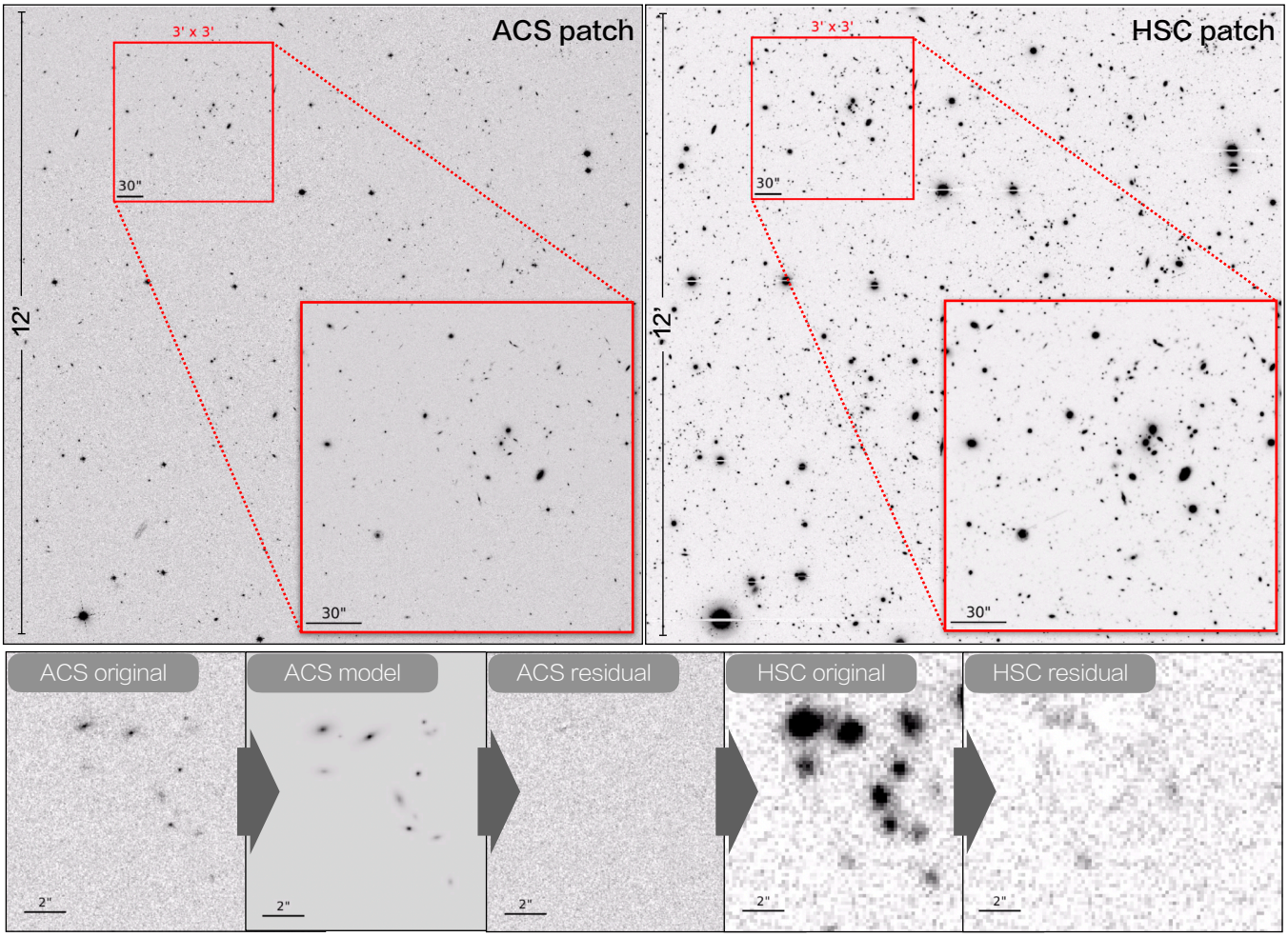

Figure 6. Illustration of our prior-based photometer approach with TRACTOR. The top large panels show the $12' \times 12'$ *patches* of the ACS and HSC observations. The inset shows a $3' \times 3'$ region, which is the size of a *sub-patch*. The bottom row of panels shows different stages of our approach. From left to right these are *(i)* original ACS image, *(ii)* ACS model image created with TRACTOR, *(iii)* ACS residual image (original minus model), *(iv)* HSC original image, and *(v)* HSC residual image after convolving the ACS models with the difference in the PSFs and scaling to the HSC images of the sources. This prior based approach has the advantage that it can efficiently deblend sources when applied to deep, low-resolution images.

and does not suffer from morphological $k-$correction. Since TRACTOR can fit nearby sources of light simultaneously, this forced-photometry approach is valuable in fields with high confusion or blending. Second, because of the parametric fitting approach and the inclusion of the PSF (in the model step), TRACTOR provides PSF-corrected total fluxes for the fitted objects; this is especially valuable to extract the contribution of low surface brightness regions beyond the isophotal size of objects.

On the other hand, there are regimes where the performance of TRACTOR is significantly reduced. Although TRACTOR provides a variety of models to parameterize the light distribution, including a point source (i.e., $\delta-$functions), a simple Gaussian, Sersic models, and even multi-Gaussian representations, it would fail to measure robust fluxes of non-smooth light distributions. Examples are galaxies with extended spiral structure, or galaxies with bulge and disk components (specifically when fit with a single Sersic profile).

As we demonstrate through simulations, we found that for our scientific goal (measurement of the photometry of compact sources), TRACTOR results in accurate photometry. However, we compare its performance to another extensively used photometry package called TPHOT (Merlin et al. 2015, 2016) which is currently being upgraded in preparation for *Euclid* joint photometry. This is presented in Appendix A of this paper.

3.1. *ACS and HSC Photometer Pipeline*

Our pipeline takes as input an ACS and HSC *patch* together with the corresponding PSF (Section 2.4) and astrometric shifts between the images (Section 2.3). It then runs TRACTOR on the ACS image to create a para-

metric model for each source in the image. The model for each source is then convolved by the (positional dependent) HSC PSF and scaled to fit the data in the HSC image (see Figure 6). We detail the different steps in the following. Multiple *sub-patches* are processed in parallel (see Appendix B).

Step 1 - Preparation. We first cut a $3' \times 3'$ *sub-patch* with $10''$ overlap from the HSC *patch* together with the corresponding ACS *sub-patch*. The overlap ensures a good fitting of sources at the edges. To keep the World Coordinate System (WCS) information, we are using the Python command `Cutout2D`. The following steps are applied to a single *sub-patch*.

Step 2 - Obtain positions and preliminary shapes. We first run SExtractor on the ACS image. This provides the locations of the sources as well as initial shape parameters (such as `A_IMAGE`, `B_IMAGE`, `FLUX_AUTO`, `FLUX_RADIUS`, and `THETA_IMAGE`) which are needed as initial guesses for Tractor. It also produces a segmentation map which identifies the pixels out to the isophotal radius of each source. The ACS data has very few repeats per pixel on the sky as a result of which there are residual cosmic rays in the mosaic. We perform a removal of such spurious sources in the SExtractor catalog, which are characterized by sizes smaller than the diffraction limit, with `FLUX_RADIUS` < 1.7 ACS pixels. We found that this cut removes most cosmic rays ad spurious sources clustered at the edges of the ACS coverage.

Step 3 - Obtain ACS models and photometry. Tractor is run on each source extracted in step 2. Specifically, we create a cutout for each source using the SExtractor `XMIN`, `XMAX`, `YMIN`, and `YMAX` keywords. We increase the size of this cutout by 50 percent and fit all objects within this cutout (also the ones not covered entirely) simultaneously. It is important to distinguish between unresolved and resolved sources for obtaining the best possible fits. Specifically, unresolved sources (or point sources) are fit using Tractor's *PointSource*[5] class. All other sources are fit using the *SersicGalaxy*[6] class. We assign a point source flag to all sources with either *(i)* `CLASS_STAR` greater than 0.8, brighter than 23 mag, and axis ratio[7] greater than 0.8, or, *(ii)* fainter than 23 mag, axis ratio greater than 0.8, and half-light radius smaller than the F814W PSF FWHM. The parameters measured by SExtractor in step 2 and a Sersic index $n = 2$ are used as initial guesses. The Tractor *Image* object is created using the *PixelizedPSF* class, which converts the input PSF from *FITS* format to a format suitable for Tractor. Furthermore, we feed in the per-pixel-noise measured from a 3σ clipping on the image. The background is fixed at zero-level as the images are background subtracted. During fitting, we allow the position to wander within ± 1 px (corresponding to ± 30 mas) from its initial guess. All other parameters, except the position angle (given by `THETA_IMAGE`), are set free to vary.

Step 4 - Forced photometry on the HSC image. Finally, the best-fit parameters (position, flux, and shape parameters in the case of resolved sources) obtained in step 3 are used to photometer the HSC image. In a similar manner as in the previous step, cutouts of each source are created. However, as we expect significant blending and confusion compared to the ACS image, we cannot simply take the segmentation image created in step 2. Instead, we first run SExtractor on the HSC image and enlarge the resulting segmentation map by convolving it with a $1''$ boxcar filter. This will combine the segmentation areas of close-by objects, creating one single large area [8]. From this, we recalculate the `XMIN`, `XMAX`, `YMIN`, and `YMAX`. For each source in the ACS Tractor catalog (from step 3), we check in which enlarged segmentation area it falls and create a cutout accordingly. All sources within this cutout are fit simultaneously using their ACS position and shape priors. If no segmentation area was found (e.g,. due to faintness or color gradient), we apply a $2'' \times 2''$ cutout size. Note that we add the astrometric offsets between the HSC and ACS images obtained in Section 2.3 to the ACS prior position in this step. During the fit, we allow the positions to vary within ± 0.5 px (corresponding to ± 84 mas) and fix all other parameters except the total flux. We note that because we are applying a median astrometric offset between the ACS and HSC images per *patch*, allowing the positions to vary a small amount is crucial to account for astrometric scatter.

Figure 7 shows the histograms of the pixel flux distribution on the original HSC image as well as the residual image after fitting all sources with Tractor. While the original image (blue line) shows a tail towards positive fluxes (these are the detected sources), the residual image (orange line) is in good agreement with the expected noise distribution (simulated uniform Gaussian noise across image without sources). There is a small imbalance on the residual image towards negative fluxes,

[5] The *PointSource* class requires a position and total flux.

[6] The *SersicGalaxy* class requires a position, total flux, axis ratio, position angle, half-light radius, and Sersic index n.

[7] In the following, defined as the ratio of `B_IMAGE` and `A_IMAGE`.

[8] Note that the resulting segmentation map is a binary map as the knowledge of pixel ownership for the extracted sources is lost in the convolution step.

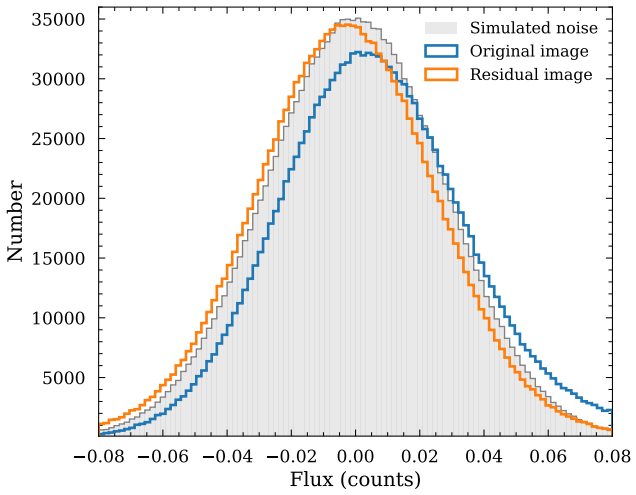

Figure 7. Comparison of the pixel flux distribution on the original HSC image (blue) and the residual HSC image after photometering with TRACTOR (orange). The gray histogram shows the expected distribution for uniform noise across the image. The peak of the residuals is shifted slightly negative which indicates a slight "over subtraction" of sources (i.e., over estimation of flux).

which could hint towards a slight over-subtraction of fluxes by TRACTOR. Statistically, this offset is less than 0.01 mag at 25.5 mag.

Appendix B provides a detailed descriptions of the setup and the process to run the pipeline efficiently at NERSC.

3.2. *Simulations*

We create simulated images to demonstrate the performance of TRACTOR as well as to compute sensitivity limits and detection completeness. The simulated images are created with SKYMAKER[9] (Bertin 2009), which allows the creation of point sources as well as multi-component bulge+disk galaxies with different shape properties. For the multi-component galaxies we assume a range of shape parameters typically observed in $z < 3$ galaxies (Bruce et al. 2014). Specifically, we assume for the Sersic $n = 1$ disk, a scale radius $0.1'' < R_{\rm disk} < 1.0''$, a disk axis ratio between 0.3 and 0.9, and random orientation. A Sersic $n = 4$ bulge is added with a bulge-to-total ratio (BTR) between 0.2 and 0.9, a scale length varying between $0.2 - 0.5$ times $R_{\rm disk}$, an axis ratio between 0.5 and 1.0, and a position angle within 10 deg of the orientation of the disk. The total magnitude of the model galaxy is drawn randomly from a half-normal distribution with faint cut-off at 27 mag and $\sigma_{\rm half-normal} = 3$ mag.

[9] https://www.astromatic.net/software/skymaker

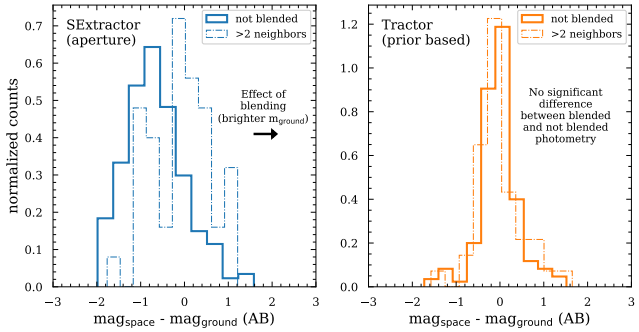

Figure 8. Comparison of the effect of blending on the photometry of sources obtained with classical aperture/auto-magnitude methods (here using SEXTRACTOR, left) and shape/position prior-based method using TRACTOR (right). This test was done using a simulated $3' \times 3'$ *sub-patch* region created with SKYMAKER with a $0.1''$ PSF (space) and $0.7''$ PSF (ground) (see text for details). The solid and dashed histograms on both panels show the space vs. ground magnitude difference for isolated source (not blended) and blended sources (with more than 2 neighbors withing the PSF FWHM), respectively. A shift towards brighter ground magnitudes is observed in the case of SEXTRACTOR for the sources with neighbors, which is the expected effect of blending. The photometry of the same sources obtained with TRACTOR does not show a significant shift, showing how prior-based photometric measurements are superior in measuring the photometry of blended sources. Note that the underestimation of fluxes in the case of non-blended sources measured by SEXTRACTOR is mostly due to loss of flux in faint, extended sources because of their low surface brightness.

3.2.1. *Demonstration of Deblending with* TRACTOR

We first use our simulation to demonstrate the benefits of TRACTOR over classical photometer codes in extracting the photometry of blended sources. Specifically, we create a $3' \times 3'$ simulated space+ground *sub-patch* image pair with the same noise properties as the real ACS and HSC images, respectively. Note that here and in the following simulations we assume equal ACS and HSC magnitudes, meaning a color of zero for each simulated object. For the purpose of demonstrating deblending and quantifying photometric accuracy, the exact shape of the energy distribution of the simulated sources is not important. We use a Gaussian PSF with FWHM of $0.1''$ and $0.7''$ for the space and ground image, respectively. To facilitate the analysis and to isolate the effects of blending, we fix the pixel scale to $0.06''$/px for both images. To ensure a statistical sample of blended sources, we adopt a source density of ~ 1500 sources per square-arcminute, which is approximately $12 - 15$ times higher

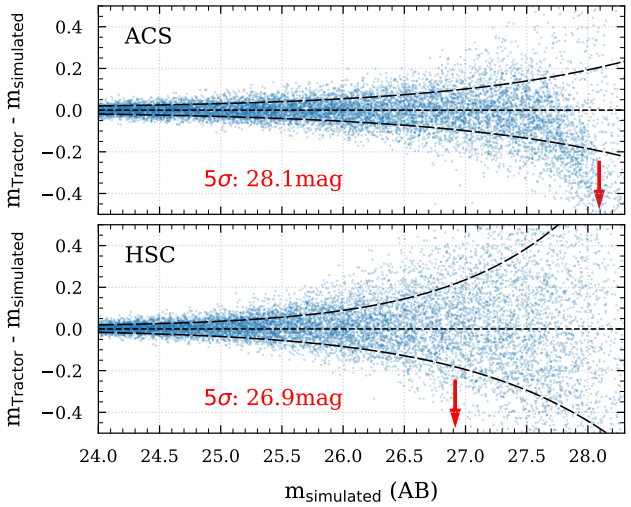

Figure 9. Recovering accuracy of ACS (top) and HSC (bottom) point source magnitudes as a function of simulated magnitude. The dashed lines denote median and 68% confidence interval. The red arrow marks the 5σ point source sensitivity limit using priors to force point source fits.

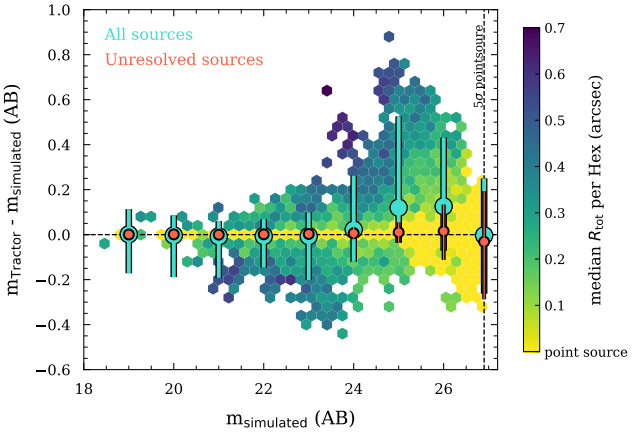

Figure 10. Accuracy of prior-based photometry measured on ground-quality images as a function of simulated magnitude and total source size (color, point sources are yellow). The details of the simulation is described in the text. The cyan symbols with error bars show the 1σ scatter for all simulated sources, while the orange symbols with error bars show the scatter of point sources. From this, we measure a 5σ point source limit of 26.9 mag. Further, the typical surface brightness dimming effect is evident.

than the average on the COSMOS field at these magnitude limits. We mix 80% of multi-component galaxies with 20% of point sources. The simulated images are then run through our pipeline in the same way as real images. To compare the result to classical methods, we run SExtractor in "dual mode". This means we use the simulated high-resolution image as detection image and measure the fluxes in apertures on the low-resolution image. We use the auto magnitudes for the correction to total fluxes.

Figure 8 shows the results of this test by comparing the magnitudes measured on the space and ground images for objects that are not blended (solid histogram) and objects that are blended (i.e., have a neighbor within the FWHM of the ground PSF, dashed histogram). The left and right panel show the results from SExtractor and Tractor, respectively. The effect of blending is clearly visible for the classic method. It leads to a significant shift of the $(\mathrm{mag}_{\mathrm{space}} - \mathrm{mag}_{\mathrm{ground}})$ distribution to $0.5-1$ mag brighter $\mathrm{mag}_{\mathrm{ground}}$ for sources that are blended. On the other hand, the same test on the same objects using Tractor results in no significant difference between blended and not blended objects. Note that the offset of unblended sources to fainter fluxes from the SExtractor measurements may be caused by the loss of flux in the wings of faint, extended sources due to their low surface brightness. This shows the advantage and necessity of using shape/position prior-based photometry measurements in minimizing the effect of blending and surface brightness effects.

3.2.2. *Photometric Accuracy and Sensitivity Limits*

We first compute the point source sensitivity limits of the ACS and HSC images by simulating 15,000 isolated point sources with SkyMaker. The pixel noise properties of the simulated images match the ones of the ACS and HSC images. Figure 9 shows the recovering accuracy of point source fluxes of ACS (top) and HSC (bottom) by Tractor using our pipeline as a function of simulated magnitude. We find no significant bias towards brighter or fainter magnitudes. This would not be the case for SExtractor without adjusting the measurements to total fluxes. The 5σ point source sensitivity limit is then estimated to be 28.1 mag and 26.9 mag for ACS and HSC, respectively, based on where the scatter in accuracy is greater than $0.21 = 2.5/\ln(10)/5$. We note that these are slightly improved compared to a blind point source search since we have used prior positions to fit for the sources.

To quantify accuracy of our photometric measurements as a function of galaxy size, we simulate a $10' \times 10'$ ACS+HSC image pair using SkyMaker. We simulate galaxies in the parameter space defined above, with 80% extended sources and 20% point sources. We assume a source density of 120 sources per square-arcminute, which is common for the COSMOS field at these magnitude limits. The image pair is then run through the pipeline. Figure 10 shows the accuracy of the Tractor magnitude as a function of the input (simulated) magnitude. The colored hexagons show the light-weighted

median radius[10] of the simulated galaxies. This shows that TRACTOR can recover the fluxes of compact objects better than for extended objects. As mentioned in the beginning, this is not surprising as more extended galaxies with a bulge and disk component are not well fit by a single Sersic model. Furthermore, at faint magnitudes even TRACTOR underestimates the fluxes of extended objects as it misses to recover the disk component due its lower surface brightness. Generally, we do not find significant biases down to the 5σ point source sensitivity for compact galaxies. On the other hand, the fluxes of more extended sources are being underestimated systematically at > 25AB by $\sim 0.1 - 0.2$ mag on average. Given confusion and faintness, they are still less biased than, for example, `SExtractor` aperture measured fluxes (c.f. Figure 8).

As we photometer the HSC image using an ACS prior, the detection completeness of our catalog depends on the detection on ACS image entirely. The latter is performed by SEXTRACTOR. It is therefore straight forward to compute the overall detection completeness for point sources. To do so, we simulate a $8' \times 8'$ ACS image with a grid of point sources with varying magnitudes down to 29 mag. The background noise was set to match the one of the real ACS images. We then run SEXTRACTOR on the image with the same parameters as used in our pipeline. We find the detection completeness is 100% down to 26.7 mag and decreases to 90% at 26.9 mag, which is the 5σ point source limit of the HSC images.

4. SELECTION OF QUASARS CANDIDATES

Quasars at high redshift can be identified primarily by their compactness and color. Quasars should be point-like and therefore unresolved, even in space-based observations. Furthermore, the ACS F814W filter extends redward of the Subaru/HSC i-band filter, which allows the measurement of the flux difference across rest-frame wavelengths of 1216 Å (see top panel of Figure 1). For quasars (or any high redshift galaxy) a red color is expected due to the drop in flux caused by the Lyα forest (absorption of ionizing photons by intervening neutral Hydrogen).

In the following, we describe the selection of our high-redshift quasar candidates in more detail.

4.1. *Selection by Color and Compactness*

First, we perform a selection of high-z quasars from the joint catalogs, based on color and compactness.

[10] We define $R_{\rm tot}$ here as the light-weighted median, i.e., $R_{\rm tot} = (1 - {\rm BTR}) \times R_{\rm disk} + {\rm BTR} \times R_{\rm bulge}$

The top panel of Figure 1 shows the spectral energy distribution from the stack of quasars in the Sloan Digital Sky Survey (SDSS, York et al. 2000; Eisenstein et al. 2011; Blanton et al. 2017) redshifted to $z = 6.2$ and with intergalactic medium (IGM) absorption applied (Madau et al. 1999). Also shown are the bandpasses of the ACS/F814W and HSC i-band filter. The bottom panel shows the expected evolution in [HSC-i]−[F814W] colors for the same quasar template at different redshifts, normalized to a rest-frame $B-$band luminosity of $10^{45}\,{\rm erg\,s^{-1}}$. Note that luminosity (an unknown parameter here) does not affect the color, only the value on the y-axis.

We therefore apply an initial [HSC-i]−[F814W] color cut of > 0.5 mag, which selects objects between redshifts $5.9 \leq z \leq 6.8$. Note that this selection also removes stars of spectral types earlier than L5 (even dust obscured, see Figure 1), which are spatially unresolved and therefore would pass the compactness criteria. The contamination by cooler stars will be discussed in Section 4.5. For the color selection, we include the uncertainties and limits of the magnitude measurement as well as a 3σ clearance. Specifically, we require

$$m_{\rm HSC} - m_{\rm ACS} > 0.5 + 3 \times \sqrt{\sigma^2_{\rm HSC} + \sigma^2_{\rm ACS}}, \quad (1)$$

where $\sigma_{\rm HSC}$ and $\sigma_{\rm ACS}$ are the 1σ uncertainties on the HSC-i and F814W magnitudes, respectively. For HSC-detected sources, we take the 1σ flux errors output by TRACTOR. For sources detected at less than a S/N of 5, we assume the 1σ limit measured from our simulations (Section 3.2.2) for a S/N= 5 source. Note that galaxies or quasars at $z \geq 6$ should generally not be detected in the HSC i-band (they are so-called i-band dropouts). To be most inclusive in our initial selection, we include sources detected in HSC-i, which will later be removed in our final visual inspection (Section 4.2).

LBGs, as well as strong emission line galaxies at lower redshifts (such as [O III] at $0.72 < z < 0.88$), will have similar colors and therefore could be included in this selection. We estimate that the latter would result in [HSC-i]-[F814W] colors of ~ 0.2 or less, hence would be excluded by our color cut. Furthermore, LBGs and low-z galaxies would be more spatially extended than quasars given the high resolution of the HST observations (see Section 4.4). We therefore require an additional cut in ACS size.

Specifically, we select sources that are compact and unresolved on the F814W images. In the following, we use the SEXTRACTOR-derived `CLASS_STAR`, `FLUX_RADIUS` (half-light radius), and axis ratio to perform this selection. From our point source simulations described in Section 3.2.2, we find that SEXTRACTOR's

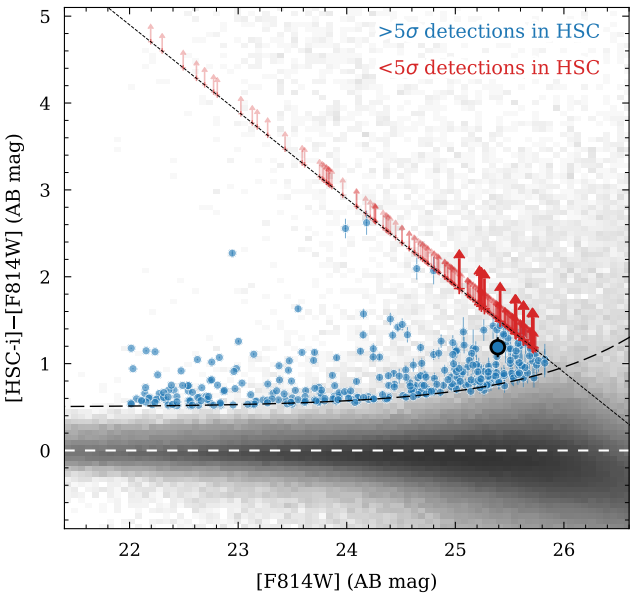

Figure 11. Initial [HSC-i]−[F814W] color selection. The color symbols show the 555 galaxies in the initial selection by color and compactness. The blue points are $> 5\sigma$ detected in HSC-i, while the red arrows denote non-detections. The final sample of 12 candidates is indicated in stronger colors. The gray background cloud shows all extracted sources in our Tractor catalog. The long-dashed line shows Equation 1, assuming the theoretical relation between magnitude uncertainty and 1σ limit. The dotted line shows the 5σ point-source limit in HSC-i.

star classification neural network can reliably tag point sources with `CLASS_STAR` > 0.9 down to a magnitude of 25.5 mag. For fainter magnitudes, `CLASS_STAR` > 0.5 includes point sources, but with a significant amount of contamination from extended sources. We therefore add an additional `FLUX_RADIUS` cut of 3 ACS pixels, which corresponds to the average PSF FWHM. In addition, we require an axis ratio (`B_IMAGE`/`A_IMAGE`) of > 0.8, which, according to our point source simulations, is expected for point sources brighter than 27 mag in F814W.

After applying these two selection criteria, we remove sources at the edges of the ACS coverage, which likely are spurious due to the reduced number of frames causing lower sensitivities and less reliable cosmic ray/artifact removal. We end up with a sample of 555 sources, which are shown in Figure 11, along with the other objects in our Tractor catalog.

4.2. *Visual Inspection*

Next, we visually inspect the ACS and HSC images and the corresponding Tractor residuals of the 555 candidates. The main purpose is to remove obvious stars from our sample and to ensure a non-detection in HSC-i

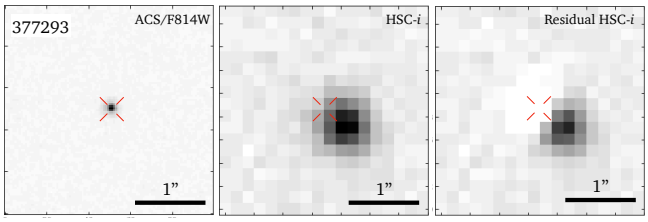

Figure 12. Example of a 23 mag star with significant proper motion ($\sim 15\,\mathrm{mas\,yr^{-1}}$ measured between 2004 and 2015). This star was included in our selection due to the underestimation of the HSC-i flux by Tractor. The latter is introduced by semi-fixed prior positions.

and bluer bands. The latter is expected for quasars and galaxies at $z > 6$.

We notice that some stars with proper motion are included in our candidate selection due to an underestimated flux measurement in HSC, hence resulting in a red color. This is because we let the prior position centroid only vary by ± 0.5 HSC pixels (corresponding to about 80 mas) to improve deblending, hence stars with proper motions of more than $\sim 8\,\mathrm{mas\,yr^{-1}}$ (80 mas over the 10 year baseline of ACS and HSC) are expected to be fit poorly by Tractor. Figure 12 visualizes this in the extreme case of a 23 mag star with a proper motion of roughly $\sim 15\,\mathrm{mas\,yr^{-1}}$.

To ensure a non-detection in HSC-i and bluer bands, we created stacks of the ancillary data in various broad-band and narrow-band filters, which we downloaded directly from IRSA. Specifically, we create two stacks; a "blue" stack including the Subaru B, V, r, g, and $NB816$ (narrow-band) bands, and a "red" stack consisting of the Subaru $z-$band and the UltraVISTA Y, J, H, and $K-$band filters. If the sources are truly at high redshifts, the blue stack should result in a non-detection. We therefore exclude candidates that have a visual detection in the blue stack as well as the HSC-i filter. On the other hand, a detection in the red stack is possible and could serve as confirmation that the source is real, despite the significantly reduced sensitivity in those bands. For example, a $z = 6.0$ source with $25 - 26$ mag in F814W would be expected to be detected at $24 - 25$ mag in the UltraVISTA filters according to a constant star formation Bruzual & Charlot (2003) template. We therefore do not impose any selection criteria on the red stack.

Finally, we also remove some of the obvious spurious sources (such as objects on the edges of the field or diffraction spikes of stars) and candidates with unreliable photometry where the contribution from a bright foreground source could not be accurately removed.

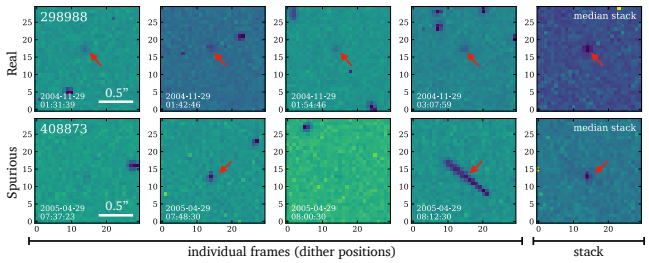

Figure 13. Example of a real source (top row) and a spurious source (cosmic ray, bottom row). The left four panels show the individual frames (i.e., dither positions, date and time of observation are indicated). The right-most panel shows a simple median stack of the individual frames. The red arrow marks detections. We remove sources from our candidate sample if they are detected in less than three frames.

After this selection step, we end up with 33 candidates that obey the color cut (Equation 1), are compact, and are undetected in the "blue" stack.

4.3. *Removal of Spurious Sources (Cosmic Rays)*

Our best candidates from above are only detected in ACS/F814W and therefore may include spurious artifacts in the HST images. Specifically, due to the preference of surveying a large area, each ACS/F814W pointing on COSMOS only used a 4-point dither pattern, making cosmic ray removal more challenging. To alleviate this, we require that candidates are detected in at least 3 frames (out of 4). Note that due to the superior depth of the ACS images compared to HSC, our candidates are detected at S/N $\gtrsim$ 30 in F814W, hence should be detected in individual frames as well at a S/N $\gtrsim$ 15. Figure 13 shows an example of a real detection and a spurious detection. The latter is likely caused by a cosmic ray hit on frames two and four, while the former is at consistent flux levels in all four dither positions. After the visual inspection and rejection of spurious detections, we end up with 12 final candidates in our sample.

As an additional check, we compared the sizes of our candidates to the sizes of simulated point sources. For this, we injected 30 000 point sources at various magnitudes convolved with the F814W PSF into real ACS F814W images and extracted them using the cataloging procedure. Figure 14 shows the results of these simulations on the `MAG_AUTO` versus `FLUX_RADIUS` (half-light radius) diagram. Also shown are our 33 visual inspected candidates. At bright magnitudes, the measurements converge to the half-light radius of the PSF ($\sim$ 2.5 pixels). At fainter magnitudes, the scatter in half-light radius increases and sizes are generally underestimated due to surface brightness effects, leading to values of 2 pixels or less. Our 12 final candidates (solid blue)

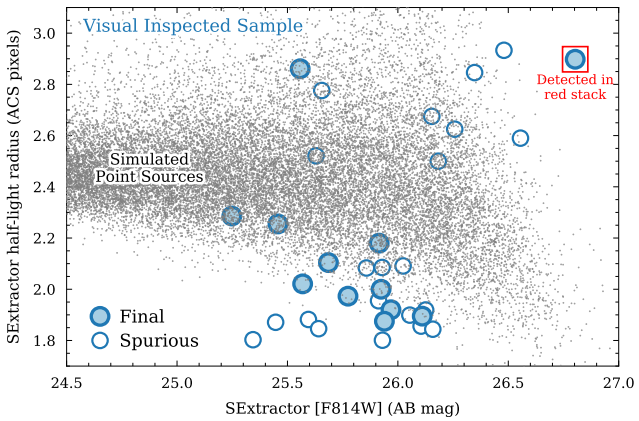

Figure 14. Visually inspected sample of 33 candidates on the `MAG_AUTO` vs. `FLUX_RADIUS` diagram. The final 12 candidates are shown in filled blue circles. Candidate 772319, detected in the red stack, is highlighted with a red box. Visually identified spurious detections (Section 4.3) are shown as empty blue circles. Simulated point sources (see text) are shown in gray.

are consistent with the scatter in the sizes of the simulated point sources, a further indication that they are real.

Figure 15 shows the 3″ × 3″ cutouts in F814W and HSC-i including the corresponding TRACTOR residuals the final sample of 12 candidate. We also show the blue and red stack for each source (see Section 4.2). None are detected in the blue stack by construction, and candidate 772319 is the only one detected in the red stack. This candidate is also detected in the latest *COSMOS2020* catalog (Weaver et al. 2021a) and has a reported photometric redshift of $z_{\rm phot} = 5.92$ (the other candidates are not in the catalog as it is based only on ground-based imaging).

The properties of the 12 candidates are summarized in Table 1.

4.4. *Size Comparison to Galaxies at similar redshift*

Quasars, outshining their host galaxies, are expected to be unresolved point sources even in observations with space-based observatories such as the HST. In Figure 16 we compare the PSF-corrected half-light radii of our candidates (red) to $z \sim 6$ galaxies from the literature (gray), which would have similar [HSC-i]-[F814W] colors. We report the median sizes with scatter of narrow-band selected Lyα emitters (LAEs) at $z \sim 5.5$ (Paulino-Afonso et al. 2018) and i-band dropouts ($z \sim 6$ LBGs Mosleh et al. 2012). Generally, both measurements (especially the one of the LAEs) suggest sizes considerably larger than for our candidates. However, it is to note that while the former study measures the sizes on F814W images, the latter uses WFC3/IR F160W. Fur-

Table 1. Summary of candidates.

ID	R.A. (J2000)	Decl. (J2000)	[F814W] (AB mag)	[HSC-i] (AB mag)[a]	[HSC-i]-[F814W] (AB mag)[b]	R_e ($''$)[c]	$z_{\rm phot}$	detection in red stack
126444	150.6622	1.926	25.39 ± 0.02	26.58 ± 0.11	1.19 ± 0.11	0.04	···	×
126828	150.589	1.809	25.63 ± 0.03	>26.90	>1.27	0.04	···	×
298988	150.4077	2.7466	25.71 ± 0.02	>26.90	>1.19	0.03	···	×
303826	150.3563	2.7593	25.27 ± 0.03	26.92 ± 0.17	>1.63	0.07	···	×
342154	150.1967	2.0339	25.41 ± 0.02	>26.90	>1.49	0.03	···	×
396311	150.2752	2.5275	25.04 ± 0.01	27.55 ± 0.26	>1.86	0.05	···	×
555462	149.8889	2.238	25.24 ± 0.02	27.59 ± 0.25	>1.66	0.03	···	×
622752	149.7843	1.7169	25.22 ± 0.01	>26.90	>1.68	0.05	···	×
667155	149.6293	2.2474	25.63 ± 0.02	>26.90	>1.27	0.03	···	×
715691	149.5934	1.6758	25.56 ± 0.02	>26.90	>1.34	0.03	···	×
747548	149.5442	2.2755	25.55 ± 0.02	27.73 ± 0.36	>1.35	0.03	···	×
772319	149.4493	2.5234	25.72 ± 0.01	>26.90	>1.18	0.07	5.92[d]	✓

[a] Tractor non-detections have been replaced with the 5σ limit (26.9 mag)

[b] Limits are reported for [HSC-i] measurements at $< 5\sigma$ and Tractor non-detections

[c] PSF-corrected half-light radii

[d] Has match in the *COSMOS2020* catalog (Weaver et al. 2021a)

thermore, the images (mostly taken from deep Hubble fields) may differ in depth and reduction from the COSMOS F814W observations. Therefore we also show several samples in the COSMOS field, which allows a direct comparison to our candidates. Specifically, we show the F814W size distributions of photometric galaxies between $6 < z_{\rm phot} < 7$ (Weaver et al. 2021a), spectroscopically confirmed $z \sim 5.7$ LAEs (Shibuya et al. 2018), and spectroscopic galaxies between $5 < z_{\rm spec} < 6$ (these include also Lyα undetected galaxies, Hasinger et al. 2018). The latter are at slightly lower redshift as we would expect for our candidates. The expected size evolution between these redshift ranges is however less than 10% (see, for example, Mosleh et al. 2012). Note that all these samples are matched in apparent magnitude to our candidates. This comparison confirms the picture that our candidates, showing sizes of ~ 0.2 kpc (assuming $z = 6$), are amongst the most compact objects at these redshifts. A population of low-luminosity quasars or exceptionally compact star-forming galaxies (see Section 5) can explain this. Exceptionally dust-reddened sources at lower redshifts ($z \sim 2$) are ruled out by the unresolved nature of the candidates, and the color difference in what are essentially two overlapping bands; we estimate that low-z sources cannot be redder than 0.5 mags in these bands.

4.5. *Quantifying the Contamination by Stars*

Late-type stars are likely the major source of contaminants as they can have red [HSC-i]-[F814W] colors and are also unresolved point sources in the HST images. As discussed in the previous sections and shown in Figure 1, the applied [HSC-i]-[F814W] color cut of 0.5 mag removes stars of spectral type warmer than L5 even for an V-band extinction of 2 magnitudes - we note that this is smaller than the typical Galactic extinction in the COSMOS field. However, the same figure shows that cooler stars can enter our selection.

Removing stars by their proper motion is not possible in our case as our candidates are only detected in one single band and no other deep space-based observations pre or post 2004 are available. At bright magnitudes, Bayesian approaches using variation of light concentration relative to that of the PSF, have been successful but at faint magnitudes, due to surface brightness limitations, this is challenging to apply (Scranton et al. 2002). With the current data in hand, we can therefore only investigate the contamination of stars by quantifying their number densities as a function of spectral type and magnitude.

Figure 17 shows the expected cumulative number density of stars with spectral types cooler than L5 over the survey area in the direction of the COSMOS field as a function of F814W magnitude. The numbers are based on the volume densities obtained from Kirkpatrick et al. (2020) and the PanSTARRS I-band absolute magnitudes from the "Three Pi Survey" (Best et al. 2021). The relative volume number density of stars in the thin and thick disk as a function of scale height is based on Buser (2000), Reid & Majewski (1993), and Binney et al. (1997). We converted the PanSTARRS I-band magnitude to ACS/F814W magnitudes by computing the color of a set of real dwarf stars in the corresponding filters (Kirkpatrick et al. 2008, 2010, 2011; Burgasser et al.

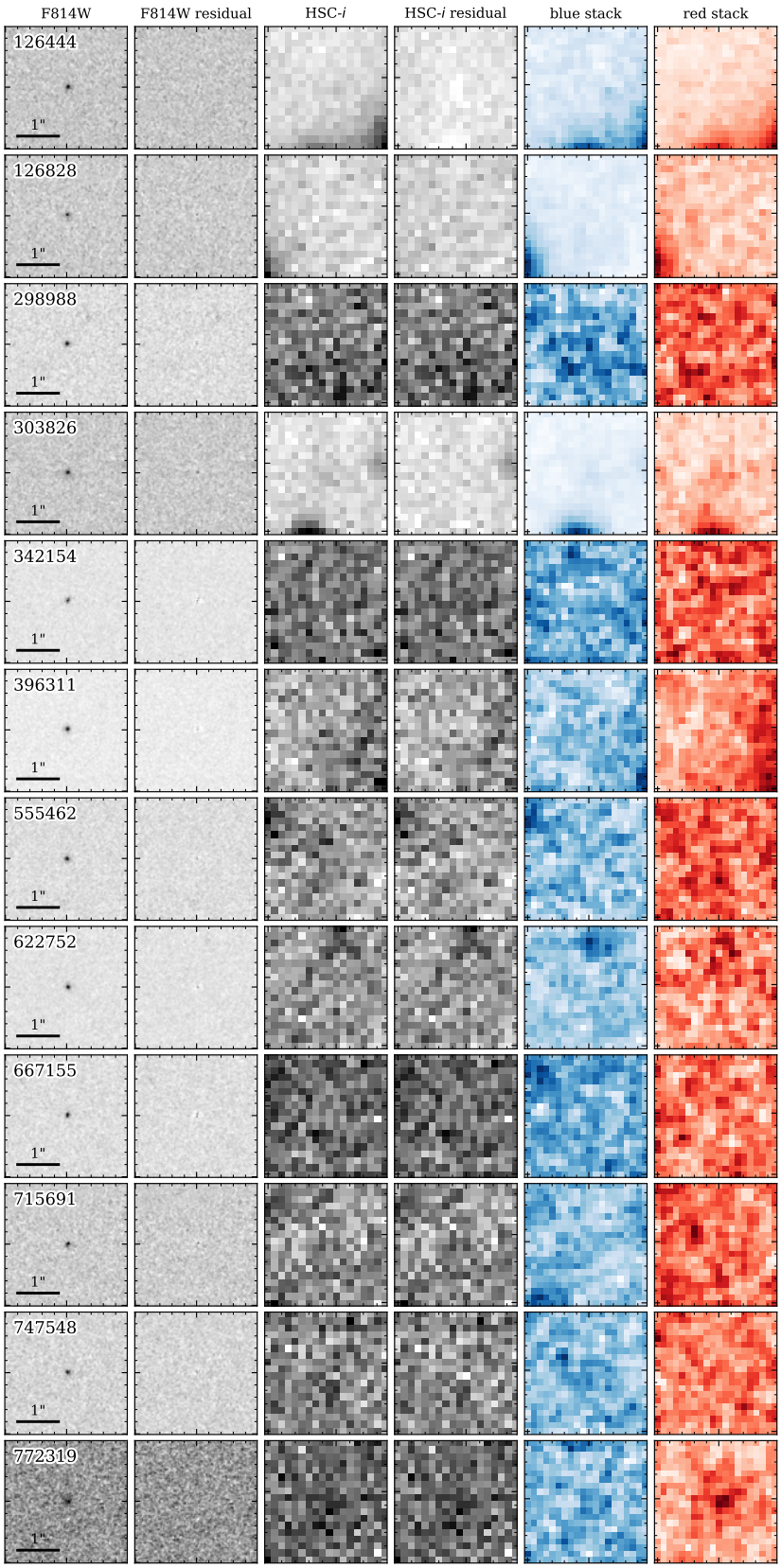

Figure 15. Cutouts of the final 12 candidates (rows). The columns show (from left to write) F814W, F814W residual, HSC-i, HSC-i residual, blue stack, and red stack. The cutouts have a size of $3'' \times 3''$, the black bar denotes $1''$. Only candidate 772319 is detected in the red stack and has a photometric redshift of $z_{\rm phot} = 5.92$ according to the *COSMOS2020* catalog. None of the candidates are detected in the blue stacks.

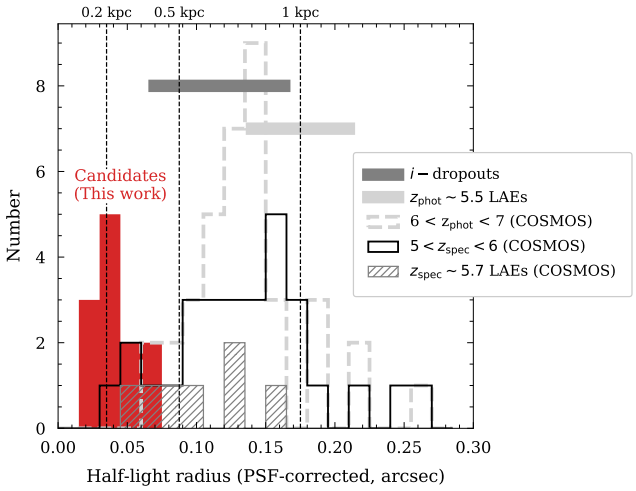

Figure 16. Comparison of PSF-corrected sizes of our 12 candidates (red histogram) with galaxies at similar redshifts selected with various methods (see text for details). We show median sizes and scatter of i-band dropouts (dark gray horizontal line Mosleh et al. 2012) and narrow-band selected $z \sim 5.5$ LAEs (light gray horizontal line Paulino-Afonso et al. 2018), galaxies selected by photometric redshifts at $6 < z_{\rm phot} < 7$ (light-gray dashed histogram Weaver et al. 2021a), spectroscopically selected galaxies at $5 < z_{\rm spec} < 6$ (black solid histogram Hasinger et al. 2018), and spectroscopically confirmed LAEs at $z_{\rm spec} \sim 5.7$ (light gray hatched histogram Shibuya et al. 2018). The latter three samples are magnitude matched and in the COSMOS field, hence allows a comparison using a dataset consistent with that used for our candidates. This comparison shows that our candidates are amongst the most compact objects at these redshifts.

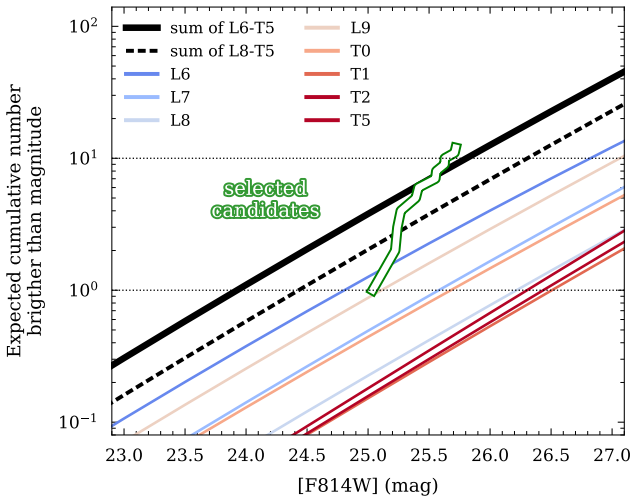

Figure 17. Expected cumulative number of brown dwarfs of different spectral types as a function of ACS/F814W magnitude. The total cumulative number of L6-T5 (L8-T6) dwarf stars is shown as a black (dashed black) line. The horizontal dotted lines show numbers of 1 and 10. The green thick line shows the cumulative magnitude distribution of the 12 final candidates.

2003, 2004, 2006, 2010)[11]. The thick green line shows the cumulative F814W magnitude distribution for our final 12 candidates. From this figure, we can see that the expected total number of L6-T5 dwarf stars over the surveyed area in our magnitude range is between 5 and 10 (thick black line). The largest contribution comes from the warmest stars of L6 spectral type (contributing $1-3$ stars). However, all our candidates have [HSC-i]-[F814W] colors of more than 1 magnitude (see Figure 11), which is too red even for L6 and L7 dwarf stars (lower panel of Figure 1). Taking this into account lowers the contamination significantly due to the lower number density of cooler stars at these magnitudes – we expect at most 3 L8 to T5 stars in our sample (thick black dashed line). Summarizing, the combination of bright magnitude, red [HSC-i]-[F814W] color cut and absence of a red "stack" detection, suggests a stellar contamination of less than 50% but spectroscopy of these sources with *JWST* will be required to confirm this.

[11] See also https://roman.ipac.caltech.edu/sims/Brown_Dwarf_Spectra.html.

5. DISCUSSION

5.1. *Number Density of Low Luminosity $z > 6$ Quasar Candidates*

Assuming that all or a fraction of our candidates are true low-luminosity quasars at $z > 6$, we can compute their number density and compare it to estimates of the QSO luminosity function derived at higher luminosities. Figure 18 shows our number density compared to quasar luminosity functions derived at $z = 5$ (McGreer et al. 2018) and $z = 6$ (Kulkarni et al. 2019) from observed data. The data points used by McGreer et al. are also shown together with an extrapolation of their double power-law fit to $z = 6$. These include the $z \sim 5$ observations by Giallongo et al. (2015) at $M_{\rm UV} > -22.8$ mag. Note that these fits are based on bright quasars at $M_{\rm UV} \leq -22.8$ mag, hence we extrapolated them to the lower luminosities where our candidates reside.

We expect a number density between $0.6 - 1.2 \times 10^{-6}\,{\rm Mpc}^{-3}\,{\rm mag}^{-1}$ if between 50% to 100% of the candidates are real low-luminosity quasars between $6.0 < z < 6.7$ (the redshift range where [HSC-i]-[F814W]> 1). This is consistent with the extrapolation to fainter magnitudes of the $z = 5$ and $z = 6$ luminosity function from McGreer et al. (2018) and Kulkarni et al. (2019), respectively. Although the data (empty gray symbols

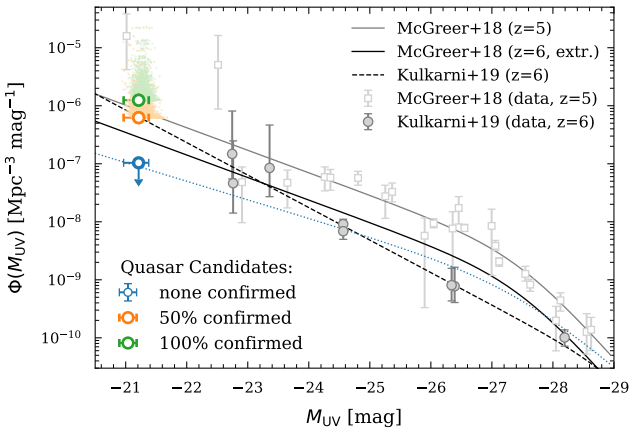

Figure 18. Constraints on the faint end of the $z \sim 6$ quasar luminosity function by our candidates. We show expected number densities for 100% (green) and 50% (orange) confirmed candidates, as well as a limit (blue) if none of our candidates are confirmed. The small circles show the distribution derived from a $V_{\rm max}$ simulation (see text). The lines show double power-law fits to $z = 5$ quasars (gray solid line, data as empty gray symbols) from McGreer et al. (2018), their extrapolation to $z = 6$ (black solid line) as well as from Kulkarni et al. (2019) at $z = 6$ (black dashed line, data as filled gray symbols). Note that these fits are derived from data brighter than $M_{\rm UV} = -22.8$. The data fainter than that (from Giallongo et al. 2015) is not used in the fits by McGreer et al. The blue dotted line is the McGreer et al. parameterization adjusted to fit the Kulkarni et al. points and our limit (blue, see text).

from McGreer et al. 2018) suggest a flattening of the number density at faint magnitudes, our observations suggest a rise. However, we find lower number densities than Giallongo et al. (2015), who cover a similar magnitude range at $z \sim 5$ by photometric redshifts of putative X-ray detections in the GOODS-S field. Note that Parsa et al. (2017), who re-analysed their data, suggest that their number densities could be up to a factor of ~ 3 lower, which would make them more consistent with our measurements at $z > 6$. If none of our candidates are confirmed, it places a firm lower limit of 0.1×10^{-6} Mpc^{-3} mag^{-1}, significantly lower than the predicted number densities from the above mentioned fits which would argue for a flattening of the low-luminosity end of the high-z quasar luminosity function.

Note that we estimated the number density of quasars by simply dividing the number of candidates by the total comoving volume between $6 < z < 6.7$. To estimate the uncertainty in this measurement given the unknown redshift of our candidates, we carried out a Monte-Carlo simulation. Specifically, we simulated 5000 galaxies assuming a flat redshift prior between $6 < z < 6.7$ and a Gaussian F814W magnitude distribution (with σ equal to the standard deviation of our candidate sample). We then used the $1/V_{\rm max}$-technique (Schmidt 1968) to derive the number density. The resulting distribution is shown as light green and orange points in Figure 18 for 100% and 50% of the candidates being confirmed as low-luminosity quasars. Faint galaxies with redshifts close to $z \sim 6$ in our Monte Carlo sample "see" a smaller volume, hence have higher $1/V_{\rm max}$ (i.e., number densities) associated with them. Assuming our candidates are equally distributed in the above redshift range, we would therefore expect our simple number density estimates to under-estimate the true number density by a factor of $3 - 4$ (corresponding to $\sim 1\sigma$ of the Monte Carlo distribution) as shown in Figure 18.

5.2. *Estimated Contribution to Reionization*

Having placed constraints on the faint end of the QSO LF, we can now calculate how much quasars contribute to the total budget of ionizing photons that led to the reionization of our universe. The answer to this question is still under debate, although it is generally thought that star-forming galaxies are the dominant contributor. The most luminous quasars likely created large bubbles of ionized hydrogen around the most massive dark matter halos. This likely increased the efficiency with which ionizing photons escape from nearby star-forming galaxies resulting in the further growth of these bubbles to encompass the entire intergalactic medium. The role of low-luminosity quasars which are in lower mass halos is therefore somewhat clear. Our measurements adds an additional data point to the low-luminosity end of the quasar luminosity function and we can make reasonable assumptions to compute the contribution of such quasars to reionization.

For our calculation, we parameterize the $z \sim 6$ luminosity function for two cases in which *(i)* 50% and *(ii)* none of our candidates are confirmed. For the first case, we simply assume the measured double power-law function from Kulkarni et al. (2019) with parameters ($\log(\phi_*/[\rm Mpc^{-3}\,mag^{-1}]$), M_*, α, β)[12] of (-10.66, -29.19 mag, -5.0, -2.4). This parameterization can reproduce our measured number density in this case (see Figure 18). For the second case, we assume the same M_* as for the McGreer et al. (2018) $z \sim 5$ luminosity function and change the normalization and slopes to fit our upper limit (see blue dotted line in Figure 18). We find parameters (-9.05, -27.47 mag, -3.3, -1.8). This results in faint-end slopes α of -2.4 and -1.8 for the two cases.

[12] Here, α is the bright-end slope and β the faint-end slope. M_* is the characteristic bend of the luminosity function.

We integrate these luminosity functions and find the rest-frame 1500Å luminosity density from these compact sources down to $M_{UV} < -21$ mag at $z \sim 6.4$ to be 0.8×10^5 and $1.2\times10^5\,L_\odot\,Mpc^{-3}$ in the two cases, respectively. As reviewed in Chary et al. (2016), the star-forming galaxy population produces a much larger rest-frame UV luminosity density of $\sim10^8\,L_\odot\,Mpc^{-3}$. If these galaxies indeed show strong nebular line emission as inferred from their multi-wavelength spectral energy distributions, it would imply an ionizing photon production rate which is a factor of 10 higher than among star-forming galaxies in the local Universe. Even with a modest escape fraction of 10%, such galaxies can easily reionize the IGM by $z \sim 6$. If the Lyman-continuum production rate in the QSO hosts is similar, as seems to be the case based on their inferred nebular emission line properties (B. Lee & R. Chary, private communication) it implies that the faint end of the QSO luminosity function has a negligible impact on reionization although it may increase the escape fraction of ionizing photons from star-forming galaxies that are within its Strömgren sphere. We therefore conclude that even mini-quasars which are several orders of magnitude fainter than the luminous quasars that have been well characterized in earlier studies, play a relatively small role in reionization but may enhance the role of nearby star-forming galaxies depending on their clustering strength.

Furthermore, if the slope of the faint end of the QSO luminosity function is found to be steeper than what we measure it to be at $z \sim 6$, it would argue for the supermassive black holes at the bright end of the luminosity function to have formed from gas accretion onto the less massive systems (e.g Bañados et al. 2016).

5.3. *Alternative Interpretation: Unusually Compact Star Forming Galaxies?*

Current estimates of the UV luminosity function (e.g., Bouwens et al. 2015), indicate ~ 500 star-forming $z \sim 6$ galaxies in the same area and at the same magnitude as our candidates. As shown in Figure 16, most of these would be resolved in Hubble imaging. However, our candidates, as they are unresolved, could be ultra compact star forming galaxies. In that case, it would be interesting to estimate the star-formation surface density to put them in context with other galaxies at $z \sim 6$.

The estimation of a SFR is less straightforward due to the likely contamination by Lyα to the flux in the F814W filter. From the F814W magnitudes, we estimate a UV-based SFR for our candidate sample of $70^{+18}_{-10}\,M_\odot\,yr^{-1}$ using the relation between UV luminosity and SFR in Kennicutt (1998a). This estimate includes the likely contamination by Lyα in the F814W filter, which depends on the EW of the line. We estimate the fraction of flux from Lyα by creating an intrinsic spectrum including Lyα of different EWs, then applying IGM absorption, and finally convolving it with the F814W filter transmission. Assuming an intrinsic EW of 500 Å for Lyα (which is rather a conservative upper limit), we expect Lyα to contribute to about half of the measured UV flux. A more common EW for star-forming galaxies at these redshifts of < 50 Å (see Schenker et al. 2014) results only in $< 10\%$ contamination.

From Figure 16, we estimate a physical size (radius) of our candidates of 0.2 kpc (see Figure 16). From this, we estimate a SFR surface density for our candidates of $\Sigma_{SFR} = 554^{+139}_{-79}\,M_\odot\,yr^{-1}\,kpc^{-2}$. Including contamination by a Lyα line with EW= 500 Å, this number can be up to a factor 2 smaller. However, as mentioned above, this is likely an upper limit. Also, note that this estimate describes the unobscured star formation. A moderate dust attenuation of $E(B-V) = 0.1$ would result in a total SFR density that is a factor ~ 3 higher. The most likely lower limit for the SFR surface density, is therefore likely around $500\,M_\odot\,yr^{-1}\,kpc^{-2}$.

We can compare this to the value for a typical main-sequence galaxies at the same redshift. From Figure 16, typical high-z galaxies have a size of around 0.7 kpc. The average main-sequence SFR (total dust corrected) of a typical $10^9\,M_\odot$ galaxy[13] at $z \sim 6$ is at $10-100\,M_\odot\,yr^{-1}$ (e.g., Faisst et al. 2020; Schaerer et al. 2020; Speagle et al. 2014). This results in a SFR surface density of around $5-70\,M_\odot\,yr^{-1}\,kpc^{-2}$. Note that this value is well consistent with the gas mass estimated with ALMA at these redshifts (Dessauges-Zavadsky et al. 2020) assuming the Kennicutt-Schmidt relation (Kennicutt & de los Reyes 2020; Kennicutt 1998b).

This estimate indicates that our candidates, if they are compact star-forming galaxies, show a $7-100\times$ higher SFR surface densities than typical galaxies at the same redshifts, hence would themselves be interesting targets to follow up spectroscopically.

6. CONCLUSIONS

In this work, we demonstrate the power of a joint pixel-by-pixel analysis of different datasets with different depth and PSF properties. The approach of prior-based photometry mitigates issues of blending and provides robust limits for non-detections. This work is an important stepping stone towards identifying challenges

[13] Since we do not detect most candidates in near-IR bands such as UltraVISTA, we can set an conservative upper limit on stellar mass.

in the analysis steps, and paves the way for applying this method to future datasets such as from the *Rubin*, *Roman*, and *Euclid* missions. A pixel-by-pixel joint analysis of these datasets will result in precision photometric properties and enhance the science output of the individual missions. The *Joint Survey Processing* (JSP) initiative at Caltech/IPAC is working towards building the techniques and infrastructure to carry out such an analysis in the future.

In this work, we have applied JSP to a unique combination of a space and ground-based set of filters in the COSMOS field, resembling in resolution and depth the future imaging data from *Rubin* and *Roman*/*Euclid*. We use this technique to place new constraints on the number density of low-luminosity ($M_{\rm UV} \sim -21\,{\rm mag}$) quasars.

We perform a pixel-by-pixel analysis of the space-based ACS/F814W filter and ground-based HSC i-band filter using TRACTOR. Specifically,

- we use the fact that the ACS/F814W filter extends redward of the HSC i-band filter, which allows us to select galaxies at $z \gtrsim 6$ using the [HSC-i]-[F814W] colors and;
- we leverage the high spatial resolution of the space-based F814W filter to select point sources (as expected for quasars).

With this technique, we are able to identify 12 robust candidate sources. Their [HSC-i]-[F814W] colors of $> 1\,{\rm mag}$ suggest them to be between $5.9 < z < 6.7$. Their unresolved nature in Hubble imaging (average PSF-corrected half-light radius of $0.03''$ ($\sim 0.2\,{\rm kpc}$ at $z = 6$) confirms the compactness expected for quasars. Using number density estimates of L and T dwarf stars (the dominant stellar contaminants) for the COSMOS field, we estimate that these could contribute about 50% of our candidates.

Taking the potential stellar contamination into account, we estimate a number density of $0.6 - 1.2 \times 10^{-6}\,{\rm Mpc^{-3}\,mag^{-1}}$ at $M_{\rm UV} \sim -21.2$. This value could be under-estimated by a factor of $3 - 4$ given the unknown redshift as derived from a Monte-Carlo sampling using the $1/V_{\rm max}$ method. These values agree well with the expected number density extrapolated from measurements at $z < 6$ and at brighter magnitudes.

In the case of no detections, we estimate a limit at $0.1 \times 10^{-6}\,{\rm Mpc^{-3}\,mag^{-1}}$. This would be at least a factor of 3 below predicted values at $z < 6$ and would indicate a flattening of the faint end slope of the quasar luminosity function. Tracing the redshift evolution of these objects could potentially help reveal the origin of supermassive black holes in the early Universe.

The low number densities of these sources imply a contribution to reionization which is at least three orders of magnitude below that of the star-forming galaxy population. However, such sources may enhance the escape of ionizing photons from neighboring star-forming galaxies and would therefore be interesting environments to study the growth of ionizing bubbles through net-generation spectroscopy.

Alternatively, our candidates could be compact star forming galaxies at $z \sim 6$. If true, their SFR surface densities can be estimated to about $500\,{\rm M_\odot\,yr^{-1}\,kpc^{-2}}$, which is $7 - 100\times$ higher than a typical main-sequence galaxy at these redshifts at $10^9\,{\rm M_\odot}$. This would suggest an interesting but rare population of compact star-forming galaxies which future spectroscopy with *JWST* will help characterize.

ACKNOWLEDGMENTS

We thank E. Merlin for providing an updated TPHOT version and technical support. This research used resources of the National Energy Research Scientific Computing Center, a DOE Office of Science User Facility supported by the Office of Science of the U.S. Department of Energy under Contract No. DE-AC02-05CH11231.

APPENDIX

A. COMPARISON TO TPHOT

We used TRACTOR to measure photometry as it allows proper deblending by using high-resolution positional and shape priors. The use of TRACTOR with simple parametric models (as we do here) has the disadvantage that the models often do not represent the true shapes of galaxies well. This is expected to happen for bright extended galaxies with significant additional sub-structure. In principle, more complicated models can be used at a higher computational

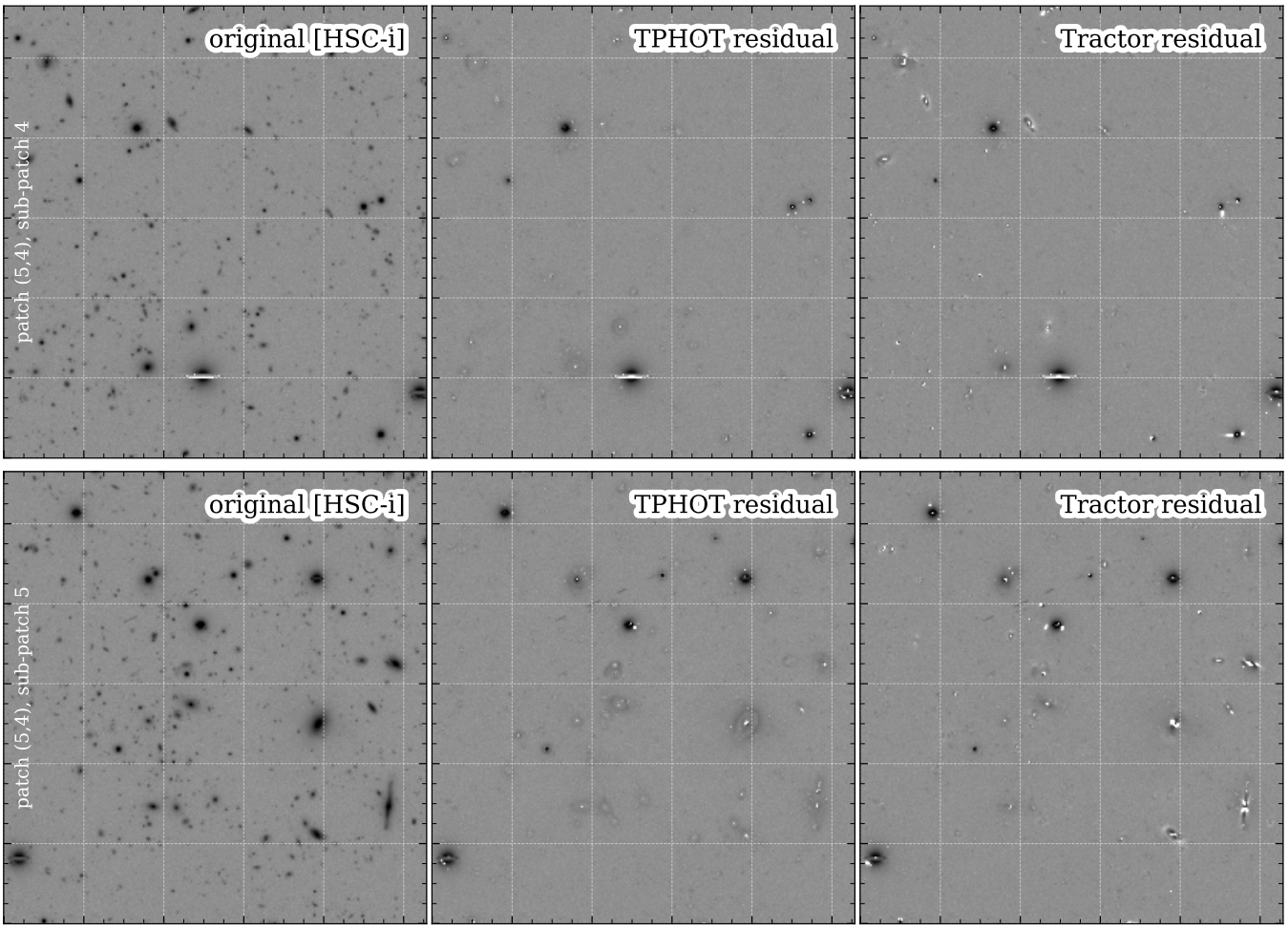

Figure 19. Comparison of Tractor (right) and Tphot (middle) residuals of two different sub-patches (top and bottom row). The original HSC *i*-band image is shown on the left. The scaling is the same in all images.

cost. Tphot (Merlin et al. 2015, 2016) offers an alternative tool to perform forced photometry measurements. Since it uses non-parametric structural models, we expect it to perform better for bright and extended galaxies.

In brief, Tphot uses the high-resolution image directly by creating cutouts of the galaxies, which are then convolved by a kernel and scaled in flux to fit the galaxies on the low-resolution image. The kernel K (on high-resolution pixel scale) has to be constructed using the low-resolution (lr) and high-resolution (hr) PSF such that $\mathrm{PSF}_{\mathrm{lr}} = K \circledast \mathrm{PSF}_{\mathrm{hr}}$. This allows Tphot to use the exact shape of galaxies as priors in a non-parametric way.

We ran Tphot on each of the $3' \times 3'$ sub-patches. We first identified sources on the high-resolution ACS/F814W image using SExtractor. To account for the different PSF sizes, Tphot creates a dilated segmentation map based on the segmentation map created by SExtractor. We chose the following parameters: *minarea_dilate* = 2.0, *maxarea_dilate* = 10000.0, *minfactor_dilate* = 4.0, *maxfactor_dilate* = 12.0, *dilation_factor* = 2.0, *dilation_threshold* = 0.0. Because Tphot requires the pixel scale of the low-resolution image ($0.168''$/px) to be an integer multiple of the pixel scale of the high-resolution image, we resized the ACS images from $0.03''$/px to $0.028''$/px. To create the convolution kernel, we took the following steps. First, we resized the HSC PSF to the new pixel scale of the high-resolution image using the function *resize_psf* from the `PhotUtils` Python package[14]. We made sure that the resulting PSF is properly normalized. Second, we used the function *create_matching_kernel* (same package) to create the convolution kernel. For the window function, we found that a top-hat filter with an inner diameter of 0.4 works best. The convolution kernel is verified by convolving the ACS PSF and comparing its profile to the HSC PSF.

[14] https://photutils.readthedocs.io/en/stable/

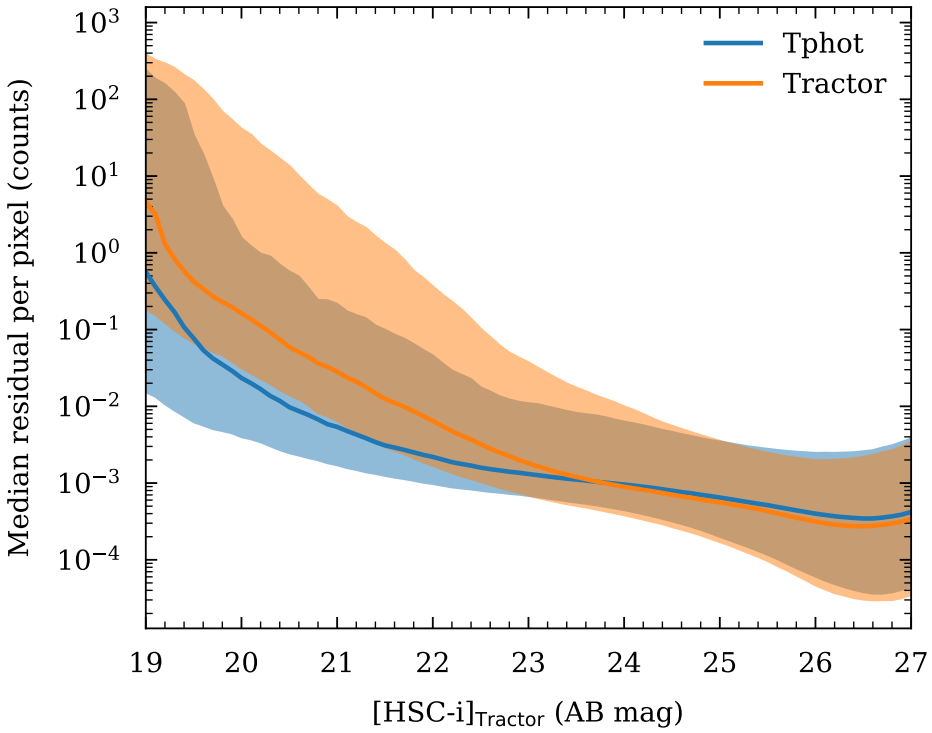

Figure 20. Comparison of TRACTOR (orange) and TPHOT (blue) per-pixel residuals as a function of [HSC-i] magnitude. The residuals of both photometry fitting methods are similar at faint magnitudes (preferentially point sources), while TPHOT is doing better for bright and extended galaxies due to its non-parametric nature. The shaded area shows the 1σ range around the median (solid lines).

Figure 19 compares the residuals from TPHOT (middle) and TRACTOR (right) for two different $3''$ sub-patches. The original HSC *i*-band image is shown on the left. While fainter point sources are fit equally well by both codes, substantial differences in the residuals can be seen for brighter extended galaxies. Specifically, the TPHOT residuals are more symmetric while the TRACTOR residuals show a "butterfly" pattern. This is because the former uses the actual shape of the ACS image while the latter is not able to capture the same amount of details in a parametric fit to the galaxies (for example a pronounced bulge + disk or spiral pattern).

Figure 20 shows this more quantitatively. For each measured source, we computed the per-pixel residual in the same aperture (defined by the segmentation map) on the residual maps produced by the different codes. The figure shows that the residuals left by TRACTOR are larger at brighter magnitude where more extended galaxies contribute. However, at fainter magnitude (dominated by compact sources), both codes perform equally well.

Summarizing, both codes have advantages and disadvantages. While TPHOT shows superior performance by reducing residuals for bright extended galaxies, both codes seem to perform equally well for compact fainter sources (> 23 mag). However, we found that TRACTOR is more versatile and faster in some cases. Specifically, the prior model fitting can be sped up by choosing a reasonable shape model (e.g., point source for faint sources, Sersic or exponential for more extended galaxies). Importantly, TRACTOR has no constraints on pixel scale or size of the images and no convolution kernel has to be created (which needs some tinkering). Furthermore, while the flux fitting itself is fast, the generation of a dilated segmentation map takes more than 90% of the total run time of TPHOT. We found that the dilation of the segmentation map is crucial in obtaining the correct fluxes as it defines the region to be fit. No dilation results in the loss of flux in the wings of sources on the low-resolution image. Furthermore, image artifacts such as diffraction spikes in the vicinity of bright stars affect the functionality of the codes and require dedicated corrections.

B. DETAILS ON THE PARALLELIZATION AT NERSC

An efficient use of supercomputing facilities will be crucial when undertaking joint pixel level analysis of 1000s of square degrees of observations. A single *sub-patch*, $3' \times 3'$ in size, with about 1500 sources, requires about 20–50

minutes to run on a high-end 2019 laptop or desktop computer. Scaling this up to something as small as the COSMOS field would require about two weeks to one month of computing time on a single desktop machine for a single pair of wavelengths. Joint pixel analysis is however intrinsically parallelizable. We made use of the supercomputer *Cori* at the National Energy Research Scientific Computing Center (NERSC[15]) to execute our pipeline.

The pipeline, written in Python, was containerized using Docker[16] and then deployed on *Cori* using Shifter[17], which is a custom software containerization solution, developed by NERSC. Shifter transforms standard Docker images into a custom format which can be used to automatically launch containers on the nodes of the supercomputer.

To deploy the pipeline on multiple nodes, we made use of a Slurm[18] batch script, as shown below.

```
#!/bin/bash
#SBATCH --job-name=JSP
#SBATCH --account=xxx
#SBATCH --time=48:00:00
#SBATCH --constraint=haswell
#SBATCH --qos=regular
#SBATCH --mail-type=BEGIN,END,FAIL,TIME_LIMIT,TIME_LIMIT_80
#SBATCH --image=docker:nrstickley/jsp_apps:2019-12-20
#SBATCH --nodes 1
#SBATCH --exclusive
#SBATCH --array=0-27
#SBATCH --output=%x_%A_%a.out

shifter /bin/bash run_jobs.sh ${SLURM_ARRAY_TASK_ID} ${SLURM_CPUS_ON_NODE}
```

This allocates an array of 28 computing nodes and launches the script `run_jobs.sh` in a Shifter container on each. Each node is labeled with integer ID number from 0 to 27, which is stored in the `SLURM_ARRAY_TASK_ID` variable. The number of logical CPU cores per node (64, in the case of Cori) is passed to the script using the variable, `SLURM_CPUS_ON_NODE`. The total time allocation per node was set to the maximum of 48 hours.

The most compute-intensive component of the pipeline, Tractor, is multi-threaded but scales poorly with core count. Running multiple instances of Tractor on each node in parallel improves efficiency, but memory consumption becomes the limiting factor. The maximum memory needed by a single task was slightly less than 16 GB. Since each Cori compute node contained 128 GB of system memory, we were able to run 8 simultaneous tasks per node. This was done using the script `run_jobs.sh`, which used GNU Parallel (Tange 2011) to efficiently distribute multiple simultaneous instances of our code across the CPU cores of each individual compute node.

```
#! /bin/bash
# run_jobs.sh runs multiple jobs on a single node.

NODE_ID=${1}  # node ID, which is the SLURM_ARRAY_TASK_ID
SLURM_CPUS_ON_NODE=${2}  # the number of logical CPUs on the node.

# define number of simultaneous jobs
njobs=8

cpus_per_job=$((SLURM_CPUS_ON_NODE / n_jobs))

echo Task ID is: ${SLURM_ARRAY_TASK_ID}

ls /path/${NODE_ID}/*.json | parallel -j ${njobs} ./task_runner.sh ${cpus_per_job} {%} {}
```

The `run_jobs.sh` script operates on a list of JSON-formatted job definition files, each of which contains all of the input parameters that our pipeline (Section 3.1) needs to run a specific *sub-patch*. There are 1008 job files, which we have distributed into 28 directories (named 0 to 27 corresponding to the node ID, `SLURM_ARRAY_TASK_ID`). GNU Parallel dynamically schedules the tasks into 8 execution 'slots' so that as soon as one task completes, another one is launched in the same slot. This continues until the full list of tasks assigned to the node has been executed.

The `run_jobs.sh` script, launches an instance of `task_runner.sh` for each job assigned to the node. The script, `task_runner.sh` handles the details of running an individual task on a set of CPU cores.

[15] https://www.nersc.gov/

[16] https://www.docker.com/

[17] https://www.nersc.gov/research-and-development/user-defined-images/

[18] https://slurm.schedmd.com/

```
#! /bin/bash
# task_runner.sh distributes the work over 8 physical CPU cores on a single NUMA node.

cores_per_task=$1  # the number of logical cores per task
slot=$2 # The execution slot; an integer from 1 to 8
filename=$3 # JSON job file for one 3' x 3' sub-patch

# This function determines which CPU threads correspond to the specified execution slot:
cpu_threads() {
    minus=$((slot - 1))
    first_cpu_thread=$((cores_per_task * minus))
    final_cpu_thread=$((first_cpu_thread + cores_per_task - 1))
    threads=$(seq $first_cpu_thread $final_cpu_thread | awk -vORS=, '{print $1}')
    echo ${threads::-1}
}

taskset -c $(cpu_threads) python runTractor.py ${filename}
```

The utility `taskset` specifies which specific logical CPU cores will be used to execute the `runTractor.py` script. This forces all of the threads of the task to remain on the same set CPU cores for the duration of their lifetime, rather than migrating to other cores over time, which improves the cache utilization and reduces the memory access latency. For the first execution slot, these would be logical cores 0-7. For the second slot, 8-15, and so on.

In summary, by distributing the jobs over 28 compute nodes, with each node running 8 jobs simultaneously, we were able to complete all 1008 tasks in slightly less than 24 hours. We plan to implement additional optimizations in the future. In particular, it is possible to run more tasks simultaneously on a single compute node by more intelligently scheduling the tasks to avoid running out of memory.

REFERENCES

Aihara, H., Armstrong, R., Bickerton, S., et al. 2018, PASJ, 70, S8, doi: 10.1093/pasj/psx081

Astropy Collaboration, Robitaille, T. P., Tollerud, E. J., et al. 2013, A&A, 558, A33, doi: 10.1051/0004-6361/201322068

Astropy Collaboration, Price-Whelan, A. M., Sipőcz, B. M., et al. 2018, AJ, 156, 123, doi: 10.3847/1538-3881/aabc4f

Bañados, E., Venemans, B. P., Decarli, R., et al. 2016, ApJS, 227, 11, doi: 10.3847/0067-0049/227/1/11

Bañados, E., Venemans, B. P., Mazzucchelli, C., et al. 2018, Nature, 553, 473, doi: 10.1038/nature25180

Becker, R. H., Fan, X., White, R. L., et al. 2001, AJ, 122, 2850, doi: 10.1086/324231

Bertin, E. 2009, Mem. Soc. Astron. Italiana, 80, 422

Bertin, E. 2011, in Astronomical Society of the Pacific Conference Series, Vol. 442, Astronomical Data Analysis Software and Systems XX, ed. I. N. Evans, A. Accomazzi, D. J. Mink, & A. H. Rots, 435

Bertin, E., & Arnouts, S. 1996, A&AS, 117, 393, doi: 10.1051/aas:1996164

Best, W. M. J., Liu, M. C., Magnier, E. A., & Dupuy, T. J. 2021, AJ, 161, 42, doi: 10.3847/1538-3881/abc893

Binney, J., Gerhard, O., & Spergel, D. 1997, MNRAS, 288, 365, doi: 10.1093/mnras/288.2.365

Blanton, M. R., Bershady, M. A., Abolfathi, B., et al. 2017, AJ, 154, 28, doi: 10.3847/1538-3881/aa7567

Bouwens, R. J., Illingworth, G. D., Oesch, P. A., et al. 2015, ApJ, 803, 34, doi: 10.1088/0004-637X/803/1/34

Bruce, V. A., Dunlop, J. S., McLure, R. J., et al. 2014, MNRAS, 444, 1001, doi: 10.1093/mnras/stu1478

Bruzual, G., & Charlot, S. 2003, MNRAS, 344, 1000, doi: 10.1046/j.1365-8711.2003.06897.x

Burgasser, A. J., Burrows, A., & Kirkpatrick, J. D. 2006, ApJ, 639, 1095, doi: 10.1086/499344

Burgasser, A. J., Cruz, K. L., Cushing, M., et al. 2010, ApJ, 710, 1142, doi: 10.1088/0004-637X/710/2/1142

Burgasser, A. J., Kirkpatrick, J. D., Liebert, J., & Burrows, A. 2003, ApJ, 594, 510, doi: 10.1086/376756

Burgasser, A. J., McElwain, M. W., Kirkpatrick, J. D., et al. 2004, AJ, 127, 2856, doi: 10.1086/383549

Buser, R. 2000, Science, 287, 69, doi: 10.1126/science.287.5450.69

Capak, P., Aussel, H., Ajiki, M., et al. 2007, ApJS, 172, 99, doi: 10.1086/519081

Chabrier, G. 2003, PASP, 115, 763, doi: 10.1086/376392

Chary, R., Petitjean, P., Robertson, B., Trenti, M., & Vangioni, E. 2016, SSRv, 202, 181, doi: 10.1007/s11214-016-0288-6

Civano, F., Marchesi, S., Comastri, A., et al. 2016, ApJ, 819, 62, doi: 10.3847/0004-637X/819/1/62

Dessauges-Zavadsky, M., Ginolfi, M., Pozzi, F., et al. 2020, A&A, 643, A5, doi: 10.1051/0004-6361/202038231

Dey, A., Schlegel, D. J., Lang, D., et al. 2019, AJ, 157, 168, doi: 10.3847/1538-3881/ab089d

Eisenstein, D. J., Weinberg, D. H., Agol, E., et al. 2011, AJ, 142, 72, doi: 10.1088/0004-6256/142/3/72

Faisst, A. L., Schaerer, D., Lemaux, B. C., et al. 2020, ApJS, 247, 61, doi: 10.3847/1538-4365/ab7ccd

Fajardo-Acosta, S. B., Kirkpatrick, J. D., Schneider, A. C., et al. 2016, ApJ, 832, 62, doi: 10.3847/0004-637X/832/1/62

Fajardo-Acosta et al., S. 2021, ApJ

Fan, X., Carilli, C. L., & Keating, B. 2006, ARA&A, 44, 415, doi: 10.1146/annurev.astro.44.051905.092514

Fan, X., Narayanan, V. K., Lupton, R. H., et al. 2001, AJ, 122, 2833, doi: 10.1086/324111

Giallongo, E., Grazian, A., Fiore, F., et al. 2015, A&A, 578, A83, doi: 10.1051/0004-6361/201425334

Hasinger, G., Capak, P., Salvato, M., et al. 2018, ApJ, 858, 77, doi: 10.3847/1538-4357/aabacf

Kennicutt, Robert C., J. 1998a, ARA&A, 36, 189, doi: 10.1146/annurev.astro.36.1.189

—. 1998b, ApJ, 498, 541, doi: 10.1086/305588

Kennicutt, Robert C., J., & de los Reyes, M. A. C. 2020, arXiv e-prints, arXiv:2012.05363. https://arxiv.org/abs/2012.05363

Kirkpatrick, J. D., Cruz, K. L., Barman, T. S., et al. 2008, ApJ, 689, 1295, doi: 10.1086/592768

Kirkpatrick, J. D., Looper, D. L., Burgasser, A. J., et al. 2010, ApJS, 190, 100, doi: 10.1088/0067-0049/190/1/100

Kirkpatrick, J. D., Cushing, M. C., Gelino, C. R., et al. 2011, ApJS, 197, 19, doi: 10.1088/0067-0049/197/2/19

Kirkpatrick, J. D., Gelino, C. R., Faherty, J. K., et al. 2020, arXiv e-prints, arXiv:2011.11616. https://arxiv.org/abs/2011.11616

Koekemoer, A. M., Aussel, H., Calzetti, D., et al. 2007, ApJS, 172, 196, doi: 10.1086/520086

Koekemoer, A. M., Faber, S. M., Ferguson, H. C., et al. 2011, ApJS, 197, 36, doi: 10.1088/0067-0049/197/2/36

Kulkarni, G., Worseck, G., & Hennawi, J. F. 2019, MNRAS, 488, 1035, doi: 10.1093/mnras/stz1493

Lang, D., Hogg, D. W., & Mykytyn, D. 2016a, The Tractor: Probabilistic astronomical source detection and measurement. http://ascl.net/1604.008

Lang, D., Hogg, D. W., & Schlegel, D. J. 2016b, AJ, 151, 36, doi: 10.3847/0004-6256/151/2/36

Lanzuisi, G., Civano, F., Marchesi, S., et al. 2018a, MNRAS, 480, 2578, doi: 10.1093/mnras/sty2025

—. 2018b, MNRAS, 480, 2578, doi: 10.1093/mnras/sty2025

Madau, P., Haardt, F., & Rees, M. J. 1999, ApJ, 514, 648, doi: 10.1086/306975

Marchesi, S., Civano, F., Elvis, M., et al. 2016, ApJ, 817, 34, doi: 10.3847/0004-637X/817/1/34

McGreer, I. D., Fan, X., Jiang, L., & Cai, Z. 2018, AJ, 155, 131, doi: 10.3847/1538-3881/aaaab4

Merlin, E., Fontana, A., Ferguson, H. C., et al. 2015, A&A, 582, A15, doi: 10.1051/0004-6361/201526471

Merlin, E., Bourne, N., Castellano, M., et al. 2016, A&A, 595, A97, doi: 10.1051/0004-6361/201628751

Mosleh, M., Williams, R. J., Franx, M., et al. 2012, ApJL, 756, L12, doi: 10.1088/2041-8205/756/1/L12

Oke, J. B. 1974, ApJS, 27, 21, doi: 10.1086/190287

Parsa, M., Eckart, A., Shahzamanian, B., et al. 2017, ApJ, 845, 22, doi: 10.3847/1538-4357/aa7bf0

Paulino-Afonso, A., Sobral, D., Ribeiro, B., et al. 2018, MNRAS, 476, 5479, doi: 10.1093/mnras/sty281

Reid, N., & Majewski, S. R. 1993, ApJ, 409, 635, doi: 10.1086/172695

Schaerer, D., Ginolfi, M., Béthermin, M., et al. 2020, A&A, 643, A3, doi: 10.1051/0004-6361/202037617

Schenker, M. A., Ellis, R. S., Konidaris, N. P., & Stark, D. P. 2014, ApJ, 795, 20, doi: 10.1088/0004-637X/795/1/20

Schmidt, M. 1968, ApJ, 151, 393, doi: 10.1086/149446

Scoville, N., Aussel, H., Brusa, M., et al. 2007, ApJS, 172, 1, doi: 10.1086/516585

Scranton, R., Johnston, D., Dodelson, S., et al. 2002, ApJ, 579, 48, doi: 10.1086/342786

Shibuya, T., Ouchi, M., Harikane, Y., et al. 2018, PASJ, 70, S15, doi: 10.1093/pasj/psx107

Speagle, J. S., Steinhardt, C. L., Capak, P. L., & Silverman, J. D. 2014, ApJS, 214, 15, doi: 10.1088/0067-0049/214/2/15

Steidel, C. C., Giavalisco, M., Pettini, M., Dickinson, M., & Adelberger, K. L. 1996, ApJL, 462, L17, doi: 10.1086/310029

Tange, O. 2011, ;login: The USENIX Magazine, 36, 42, doi: 10.5281/zenodo.16303

Trakhtenbrot, B., Volonteri, M., & Natarajan, P. 2017, ApJL, 836, L1, doi: 10.3847/2041-8213/836/1/L1

Vanden Berk, D. E., Richards, G. T., Bauer, A., et al. 2001, AJ, 122, 549, doi: 10.1086/321167

Weaver et al., J. 2021a, ApJ

—. 2021b, ApJ

York, D. G., Adelman, J., Anderson, John E., J., et al. 2000, AJ, 120, 1579, doi: 10.1086/301513